LIGHT ELEMENT ANALYSIS IN AMORPHOUS AND NANOCRYSTALLINE SILICON USING ERDA AND RELATED TECHNIQUES.

By

Olusegun Adegbite

A dissertation submitted in fulfilment of the requirements for the degree of

Master of Science

in the

Department of Physics
University of Cape Town

February, 2006

DECLARATION

I, the undersigned, hereby declare that the work contained in this thesis is my own original work and has not previously in its entirety or part been submitted at any University for a degree.

Signature **Date**

17th February, 2006

ABSTRACT

Incorporation of hydrogen and other light element impurities play a significant role in the metastability of hydrogenated amorphous silicon. In this work, investigation of light elements incorporated in the amorphous silicon network of hydrogenated and nanocrystalline silicon were analysed by using ion beam analytical techniques. To do this, amorphous silicon films were deposited by hot wire chemical vapour deposition, and a unique sampling method was developed for the analysis of nanocrystalline silicon powder. The combinations of non destructive, quantitative and sensitive Rutherford backscattering, resonance scattering and elastic recoil detection analysis were used in analysing these samples.

Oxygen was detected as the only contaminant at a concentration between 2- 6 at % in both hydrogenated amorphous silicon and nanocrystalline silicon, incorporated during and post-deposition. In the hydrogenated amorphous silicon the concentration of incorporated hydrogen was analysed by determining the hydrogen content in two states: as-deposited and after light illumination of the samples. The hydrogen content was seen to be decreasing with illumination time, indicating the role of hydrogen in the degradation of a-Si:H samples. In contrast, the hydrogen content in the nanocrystalline silicon powder was very low. The results obtained from the ion beam techniques were correlated with results from Fourier transform infrared analysis and scanning electron microscopy.

1 INTRODUCTION

Hydrogenated amorphous silicon is a material of high technological importance because of its wide electronic applications and with the opportunity of depositing it on large area using different deposition techniques, which in turn makes its production cost efficient. [1, 2, 3]. Studies have shown that nanocrystalline silicon also provides interesting properties for technological applications *e.g.* in solar cell applications, and generally in thin film technology. However, one major problem militating against the efficiency of hydrogenated amorphous silicon is its metastability [3, 4], which is a phenomenon that is still to date not well understood.

Metastability involves creation of electronic defects in hydrogenated amorphous silicon, also called the Staebler – Wronski effect (SWE) [3, 4]. The SWE is linked to the presence and the migration of hydrogen. The basic feature of creating any type of defect in a material is that an energy barrier must be overcome. This can be achieved by prolonged illumination of light, by low energy electron bombardment, by rapid quenching, by charge accumulation or by double-injection currents [4].

Concentrating on the effect of prolonged illumination in hydrogenated amorphous silicon, defect creation is attributed to coordination defects [5] and disorder in network of the amorphous structure, due to dangling bonds and vacancies. These lead to localised states in the mid band gap [6]. In pure amorphous silicon, the dangling bond density is about 10^{19} cm^{-3}, which makes the material electrically poor. The reduction of the dangling bond density to approximately 10^{15} cm^{-3} by the introduction of hydrogen to the amorphous structure improves the electrical properties [4, 5, 7, 8], *e.g.* the light/dark conductivity ratio. In light-induced metastability, dangling bonds play a dominant role because they act as recombination or trapping centres for the carriers. For instance during prolonged illumination, there is recombination of the electron – hole pairs which increases the dangling bond density and alters the Fermi level. This in turn leads to the reduction of photogenerated carriers and the increase of localised states [4]. Different models [4, 8, 9] have been proposed, in respect of this, to give an insight to this problem, but none of these models has ever been able to completely clarify this puzzle at the microscopic level.

Recent developments to create a more stable material have led to the fabrication of nanostructured materials [1], which have improved properties compared to a-Si:H. This material, which is produced by the same deposition techniques, forms a compact layer with crystalline grains in the nanoscale size range, which are embedded or connected by amorphous tissue. Such layers show little or no metastability and are highly conductive [5]. There is a decrease in non-radiative recombination (defect such as impurities, disorder sites or dangling bonds), which result in a reduction of the chance of carriers being trapped. There is also widening of the band gap, and the ratio of surface to volume atoms is increased due to reduction in size. [10]

Hydrogen has been known to also be vital in deposition of both device-quality hydrogenated amorphous silicon and nanocrystalline silicon at a certain threshold atomic percentage [2, 4]. In this research work, emphasises are on two important aspect of metastability:

- The role of hydrogen in governing both metastability and optoelectronic properties in these materials, and
- The presence and contribution of other light element impurities such as oxygen, carbon and nitrogen in these materials.

The aim of this work is to quantitatively characterize hydrogen and other light elemental impurities in a-Si:H and nc-Si, with the eventual aim of correlating these to light induced degradation phenomenon. To do this, samples have been selected in which the amorphous and nanocrystalline phases can be investigated separately. Hydrogenated amorphous silicon has been produced by hot wire chemical vapour deposition (HWCVD) under conditions in which no crystalline phase is expected. Nanocrystalline silicon is provided in the form of a powder, for which sample preparation techniques needed to be developed. The characterization of these materials is achieved by determining the hydrogen content using ion beam analytical techniques such as elastic recoil detection analysis (ERDA), Rutherford backscattering (RBS), and resonance scattering, which are correlated with other techniques. The analysis was performed in two phases: the determination of the impurity content by the RBS/Resonance scattering on both the amorphous silicon and nanocrystalline silicon samples and the determination of hydrogen content by elastic recoil detection analysis on as-deposited, illuminated samples, and nanocrystalline silicon samples.

2 AMORPHOUS AND NANOCRYSTALLINE SILICON - AN OVERVIEW

Silicon is the most abundant element in nature after oxygen, and its electronic and physical properties meet the requirement for many applications. Particularly in the semiconductor industries silicon is the most widely used material [11]. This chapter provides a general background of hydrogenated amorphous silicon (a-Si:H), of nanocrystalline silicon, and their production techniques. The role of hydrogen and other light elements impurities will also be highlighted with a discussion of the relevance of ion beam analysis to these materials.

2.1 Structural forms of silicon and their properties

For every silicon structure, whether crystalline, polycrystalline or amorphous, the basic building block is the Si-Si tetrahedron, as indicated in figure 2.1. It has to be mentioned that, in general, the structure describes the atomic arrangement [12], and that even in crystalline silicon there exist defects like vacancies, voids, impurities and dangling bonds. These defects are also found in amorphous network [5]. The dangling bonds which are predominant feature of amorphous silicon together with the strained Si-Si bonds induce a change in the binding energy and electronic state which are reflected in its properties [7].

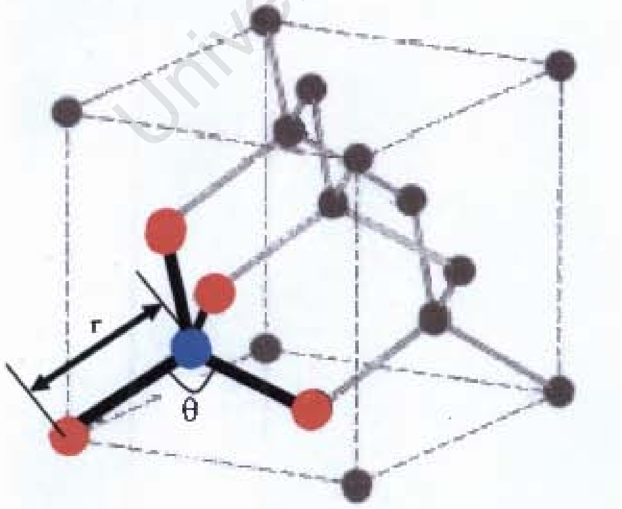

Figure. 2.1: Three dimensional model of the tetrahedral arrangement of atoms in crystalline silicon showing the diamond structure. θ and r is the bond angle and bond length respectively [12].

2.1.1 Crystalline Silicon

The crystalline form of silicon (c-Si) is a covalent semiconductor, having a long range order due to the periodic arrangement of the silicon tetrahedra in the three dimensions in space. The crystallographic structure is the diamond structure (see figure 2.1), with bond angles of 109°, and bond length of 0.27 nm. Silicon is an indirect band gap material with band gap energy of 1.1eV, which results in a low absorption coefficient of light in the UV range [13]. In contrast, in polycrystalline silicon, the long range order is maintained only inside the grains.

2.1.2 Amorphous Silicon

Amorphous silicon (a-Si) is also tetrahedrally bonded, but its structure is not based on the periodicity of the lattice as in crystalline silicon, as seen in figure 2.2. The lack of periodicity in a-Si results in a variation of bond angles and bond lengths. The average bond angle can deviate by 11.4° from the standard structure of tetrahedral bond angle, and the average bond length can differ by 1.9% from the c-Si bond length [6]. This introduces strain into the a-Si network, which results in defects, causing electronic states in the band gap near the valence and conduction band.

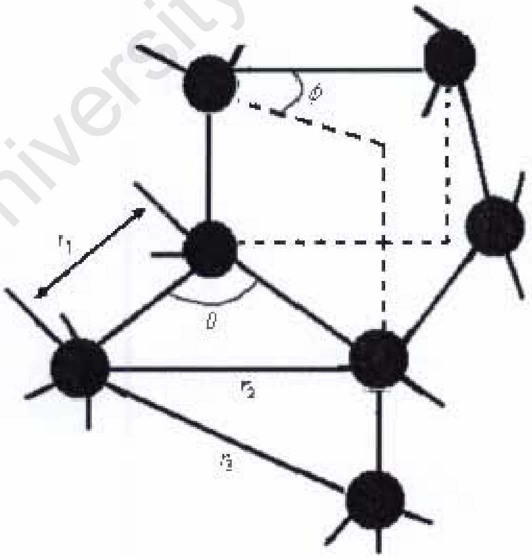

Figure.2.2: The Three dimensional model of tetrahedral amorphous semiconductor describing the structural order parameters. In contrast to crystalline silicon, the long range order is broken while the short range is retained. The co-ordination with the nearest neighbouring atoms are shown: r_1, r_2 and r_3 correspond to the interatomic distances. θ and ϕ are the bond angle and dihedral angle respectively [5].

An important defect in amorphous silicon is the dangling bond which occurs at three fold coordinated silicon atoms, *i.e.* unterminated sites, as seen in figure 2.3. Electronically, these are located at the centre of the band gap, and act as recombination centres for carriers. These results in high density of states, with dangling bond densities of the order $10^{19} - 10^{20}$ cm^{-3} for pure amorphous silicon [5], thereby make the material unsuitable for electronics application.

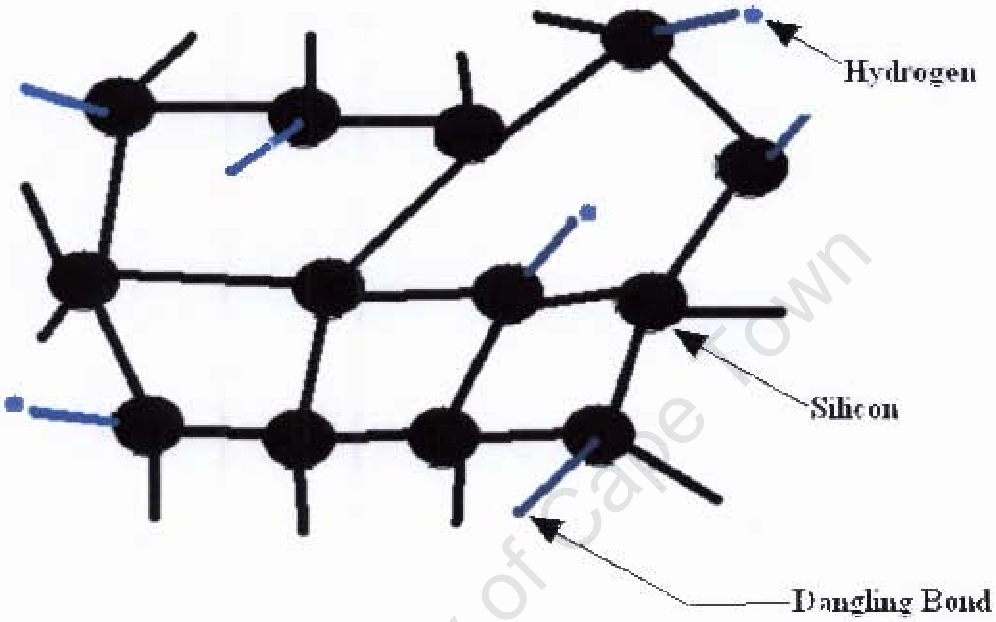

Figure. 2.3. Representation of an hydrogenated amorphous silicon structure. Silicon atoms are represented by large circles and hydrogen atoms by small circles, respectively. "Unterminated" lines indicate the dangling bonds inside the structure.[14]

To reduce the number of dangling bonds, amorphous silicon is passivated by introducing hydrogen into the structure, resulting in hydrogenated amorphous silicon (a-Si:H). Passivation of a-Si with hydrogen reduces the density of the dangling bonds drastically by causing structural relaxation [5] due to the accompanying reordering of both the bond angle and the bond length. This material now has a semiconductor nature, with a direct band gap and a band gap energy between 1.6 - 1.8 eV [13], which results in a high absorption co-efficient in the UV light range.

In spite of these merits of a-Si:H over its c-Si counterpart, a major factor militating against its efficiency is, what is referred to as the Staebler-Wronski Effect (SWE) [3]. This effect is a process of degradation of hydrogenated amorphous silicon upon illumination to light. A phenomenon that is still under investigation, studies have shown that the presence and high concentration of hydrogen and other impurities, and their complex bonding structures results in defect creation [2, 3, 4] upon illumination.

2.1.3 Nanocrystalline Silicon

Nanocrystalline silicon has an ultrafine microstructure with grain sizes in the nanoscale range, which have a high surface to volume ratio [15]. The reduction in size of the crystals has a significant effect on the overall properties of the material, for instance, changes in the band gap and physical properties. What is known as nanostructured silicon has nanoscale crystallites incorporated in an amorphous matrix [1]. Furthermore, the inclusion of nc-Si results in a better ordered matrix, with improved electronic properties compared to hydrogenated amorphous silicon [16].

Cabarrocas et al [1], in their bid to stem nanopowder formation in silane plasmas revealed the production of nanostructured films that displayed high optical absorption, and improved electronic and transport properties. Recently, compact, fully nanocrystalline layers have also been produced [17]. Therefore attention is now being shifted to nanocrystalline silicon as an alternative to crystalline silicon based devices.

In contrast to the above described nanocrystalline silicon, in this work, besides amorphous silicon, nanocrystalline powder will be investigated. The reasons for this are: Firstly, to determine the role of hydrogen in governing both metastability and optoelectronic properties in this material. Secondly, to study the presence and contribution of other light elemental impurities with the eventual aim of correlating these to the light induced degradation phenomenon.

2.2 Synthesis of a-Si:H and Nanocrystalline Silicon.

In synthesis or deposition of hydrogenated amorphous silicon many techniques are available such as plasma enhanced chemical vapour deposition, reactive sputtering techniques and hot wire chemical vapour deposition [6]. But for these studies attention is given to material produced by hot wire chemical vapour deposition.

Nanostructure synthesis techniques involve two broad approaches: The top-down approach describes the attrition of bulk coarse grained material to the nanoscale range. The bottom-up approach involves bringing together minute particles or atoms to form a macroscale material [18]. Another classification is to divide the synthesis techniques into two groups: physical methods and chemical methods [19]. Examples of chemical methods are chemical vapour deposition and chemical synthesis [20], which can be used to produce both compact layers and powder. In contrast, a physical method is mechanical attrition.

2.2.1 Deposition of hydrogenated amorphous silicon by HWCVD

The hot wire chemical vapour deposition technique (HWCVD), otherwise known as thermal catalylitic CVD was first introduced in 1979 [2]. However, the poor quality of the material deposited was attributed to a bad selection of deposition parameters [7]. Little attention was given to this technique until the late eighties when Matsumura et al [21], revealed that a device-quality material could be deposited under high pressure. HWCVD has now become a widely accepted technique for the deposition of silicon thin films. Device quality material with a low defect density and hydrogen content <10 at. % [21, 22] and even below 1 at. % [22] can be achieved. Furthermore, there is no plasma generation of reactive species, which decreases the possibility of ion-induced damage, caused as a result of ion bombardment in the growing films as in plasma enhanced-chemical vapour deposition [23]; Also large area deposition which leads to cost effective production is also possible [1,2,22].

Hot wire CVD basically involves the decomposition / cracking of precursor gases at a hot tantalum or tungsten wire (filament), at a temperature between 1600 °C and 1800°C [2]. If silane (SiH_4) gas is used, atomic silicon (Si) and hydrogen (H) which are referred to as radicals or reactive species, are produced. The radicals are then deposited on a heated substrate. Various studies have revealed that a number of reactor variables such as flow rate, substrate temperature etc, can influence the optimum growth of the film being deposited and careful selection of these parameters is important [20, 21, 24].

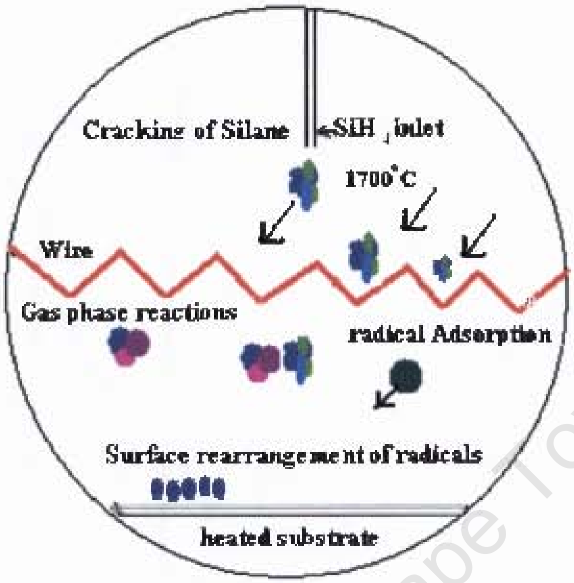

Figure2.4: Schematics of the HWCVD process, showing the various kinetics processes involved. [25]

Atul Pant et al [26], reported that the silicon film growth can be divided into four main proceses, which are also illustrated in figure 2.4:

- Silane cracking: thermal decomposition of silane and hydrogen gas into radicals which takes place near the wire surface.
- Gas phase reactions: abstraction of hydrogen to produce H_2 and SiH_3, which includes the polymerisation and disproportionation to form other species (SiH_3 and SiH_6).
- Film deposition: Adsorption of the radicals to form the film on the surface
- Surface rearrangement and insertion of these radicals and releasing hydrogen in the film growth.

At a high filament temperature there is complete decomposition of silane gas into silicon and hydrogen due to the increase in the silane consumption rate. Consequently, the hydrogen influx is increased and a rearrangement of the atom in the film surface is caused. Reduction in the filament temperature changes the morphology of the deposited material [26]. It has been shown that different catalytic materials (wire) exhibit different chemical properties with the reactive radical atoms [7]. For instance, using a tungsten wire at temperature less than 1700°C there is formation of silicides on the wire surface [27] and the film may be contaminated due to tungsten evaporation at higher temperature [28].

High flow rate and high total pressure favour the formation of radical precursors, and increase the growth rate. Hydrogen atom abstraction is increased as a result of more atomic radicals being formed. Disproportionation and polymerization, as shown in Table 1, are also more likely, resulting in the formation of higher silane (Si_2H_6) due to reaction of radicals. As the gas pressure is lowered, there is no more significant reaction in the gas phase, since the main precursor favoured then, is the Si radical, which has a high sticking co-efficient. This radical, then diffuses over the surface of the substrate maintaining the hot wire (filament) thermal energy which results in the void-rich material [28].

Table 1. Reaction model of deposition of Si films from SiH_4 [29]

1	Silane Cracking(wire)	SiH_4 ------ $Si_{(g)} + 2H_{2(g)}$
2	H abstraction (gas phase)	$SiH_{4(g)} + H_{(g)}$ ----------$SiH_{3(g)} + H_{2(g)}$
	Disproportionation(gas phase)	$2SiH_{2(g)}$ -----------$SiH_{2(g)} + SiH_{4(g)}$
	Polymerisation(gas phase)	$SiH_{2(g)} + SiH_{4(g)}$ --------$Si_2H_{6(g)})$
3	Film deposition (Substrate)	$SiH_{x(g)} + H_{(g)}$ -------$SiH_{x(ad)} + H_{(ad)}$
4	Rearragement (Substarate)	$SiH_{X(ad)} + H_{(ad)}$ ---------$Si_{(s)} +(x+1)/2H_{2(g)}$.

The influence of the substrate temperature on the crystallinity of the material is related to the mobility of the various radical species adsorbed onto the substrate surface [26]. An increase in the substrate temperature favours the mobility of the SiH_3 radical which is known to have highest mobility, and other growth radicals. SiH_3 contributes to film growth by diffusing over the surface and reacting (attachment) with dangling bonds through its movement over the surface until an energetically favourable location is reached [7]. However, due to additional heat gained by the substrate through radiation from the filament and vacuum wall chamber, the substrate temperature needs to be controlled and maintained to avoid recrystallization of the deposited material, thus losing the amorphous nature and this can be achieved by preheating the substrate to ensure a stable temperature. Good device quality material is reported to have been deposited at substrate temperature less than 400°C [28].

Hydrogen dilution has a significant effect on the film growth. Kolodziej [4] reported that above a certain hydrogen dilution level, the film being deposited becomes microcrystalline. Below this level, a structural reordering in the amorphous phase in the film is noticed. The film thickness, as well as the dilution ratio, plays an important role in morphological transition (amorphous –micro-polycrystalline film formation). A high flux of hydrogen atom improves the amorphous structure of the films. The crystallinity of the films is generally favoured by high total pressure, high substrate temperature and high filament temperature, while an increase in the silane flow rate increases the growth rate but decreases the crystalline (ordered) fraction [26].

2.2.2 Mechanical Attrition and High Energy Ball Milling

One method adopted for the production of ultrafine-grained material is rigorous mechanical working called mechanical attrition, of which high energy ball milling is an example. In general mechanical attrition to form powder particles is seen as a cold – working, non-equilibrium process under the application of high mechanical energy [18]. Figure 2.5 illustrates the process involved in ball milling of powder particles. The particles are subjected to high energy mechanical deformation by the moving balls mill. The tools balls, made of hardened steel or a ceramic such as zeconia, are placed together with the powder particles. The continuous collision during milling results in the breaking down of the coarser-grained structure. The extension of the milling period reduces the sizes, even down to the nanoscale range. The temperature produced in this process is typically below 200°C.

There is no limitation as to quantity which can be produced which makes the process industrially relevant. With ball milling for example, various nanosized powders, ranging from metal powders, such as Ruthenium [30], and amorphous powders, such as Au-Si [31] and ceramic powders such as alumina [15] were produced. Also a number of different types of mills are available e.g tumbler mills, grinding mills, or vibratory mills.

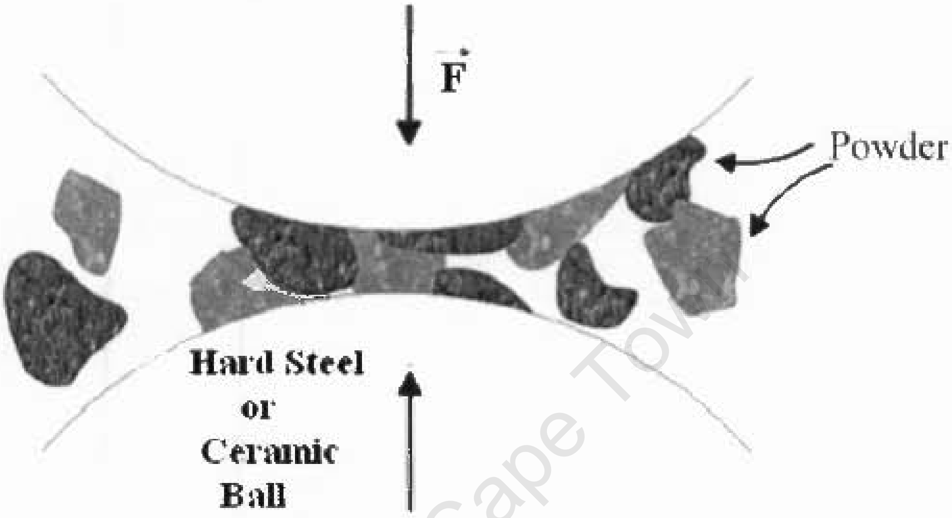

Figure 2.5: Principle of high energy ball milling process. The impact force $\vec{F}$ results from the central collision of the balls [15]

A major problem associated with milling is the contamination of the milled material, because the powder comes in contact with both the milling tools and the atmosphere during and after milling process.

Different procedures have been suggested to reduce or prevent the material from being contaminated. These include reducing the milling time, coating of the milling balls with a thin purest and most ductile metal powders which reduce contamination with Fe, and elimination or reduction of trace element concentration by sealing the powder in an inert gas compartment. Because the possibilities of contamination cannot fully be eliminated, this research work becomes especially interesting for the evaluation of silicon nanopowder produced by ball milling.

2.3 Hydrogen and Other Impurities

A major problem with amorphous silicon or any thin film material is the presence of impurities which are often unintentionally incorporated during or after deposition. Such impurities include hydrogen, oxygen, nitrogen and may be present in varying quantities in the synthesized material.

For this reason, most of the deposition and analysis techniques of thin films are often performed in a vacuum system to avoid or prevent unwanted contamination. Schropp et al [2,] reported that even if deposition of hydrogenated amorphous silicon by hot wire CVD took place in ultrahigh vacuum, the chances of contamination may be low but there is still a possibility of contamination with oxygen. Impurities may influence the electrical properties, by acting as dopants or recombination centres, but can also change structural and chemical properties [32]. Impurities have not always a negative influence but their amount have to be controlled. Like mentioned above hydrogen, which is needed for passivation of amorphous silicon (a-Si), is incorporated at a certain atomic percentage to make the material optically or electronically viable [7]. In contrast, excess of hydrogen will lead to the instability of this material and shortage causes hydrogen cluster formation [5]. In addition, hydrogen plays a significant role in the degradation of hydrogenated amorphous silicon [7], and being an important element in thin film production, thus the knowledge of its concentration is essential.

2.4 Amorphous Silicon, Nanocrystalline Silicon and Ion Beam Analysis

For the characterization of amorphous and nanocrystalline silicon a wide range of techniques are used including electrical and optical techniques [33], as well as structural methods. As previously indicated, however, a light element such as hydrogen, which plays a vital role in the structural appearance and for electrical properties of these materials, becomes cumbersome and difficult to determine. For instance, energy dispersive X-ray fluorescence analysis [34] and X-ray photoelectron spectroscopy (XPS) [35] are sensitive to most elements, but often insensitive for hydrogen analysis. The most often applied technique to determine the hydrogen content is Fourier Transform Infrared (FTIR) spectroscopy. This technique basically involves absorption, reflection or transmission of light intensity, due to interactions between incident light and the target material. The emerging light of lower intensity is expressed as a function of wavelength or frequency, which gives the characteristic of the chemical bonds present within the sample. Thus, this technique only detects and measures the bonded hydrogen in a sample. The employment of ion beam analytical techniques consisting of Rutherford backscattering, resonance scattering and elastic recoil detection analysis overcome these difficulties and provide additional valuable information about hydrogen and other light elemental impurities. In addition, total hydrogen content in a sample can be determined.

The efficiency of the combination of ion beam techniques were demonstrated in various applications, such as determination of elemental composition [36], hydrogen, nitrogen and silicon atomic concentration in dielectric silicon nitride [37], stoichiometry and areal thickness of thin multilayer amorphous semiconductor such as in, a-Si/SiO_2 [38]. Medunic et. al [33] reported about the application of ion bean analysis (IBA) techniques together with electrical and optical techniques for characterization of an amorphous silicon p-i-n structure, deposited by plasma enhanced chemical vapour deposition (PECVD). In this case the quantified total hydrogen content determined with IBA was higher when compared to that obtained with FTIR.

Hydrogen analysis in nanocrystalline silicon synthesized from silicon rich film deposited by PECVD was reported by Weijers et. al [39]. The role of hydrogen incorporation during growth to passivate the nanocrystals, which results in an significant increase of the luminescence intensity, was revealed. Gracin et.al [40] used a combination of IBA, optical spectroscopy and grazing incidence small angle X-ray scattering (GISAXS) in analysing the nanostructural properties of non-stoichiometric hydrogenated amorphous silicon carbide thin film deposited by magnetron sputtering and PECVD, in which the hydrogen content was determined and also the void volume contribution.

The capability of applying a combination of the IBA techniques to detect light elements in hydrogenated amorphous silicon deposited by hot wire CVD have not been fully exploited. This provides the frame work for the research presented in this thesis. Beside the determination of the total amount of hydrogen and other light elements in a-Si:H, ion beam techniques are for the first time, used in the analysis of nanocrystalline silicon powder. A novel preparation technique for analysis of nanocrystalline powder was developed and is described in detail in section 4.1.2.

3 INTRODUCTION TO ION BEAM ANALYSIS AND SCANNING ELECTRON MICROSCOPY

The analytical techniques used in these studies are a combination of the ion beam techniques, Rutherford backscattering spectrometry (RBS), resonance scattering and elastic recoiled detection analysis (ERDA) together with scanning electron microscopy (SEM). This chapter provides a description of these techniques starting with a brief overview of ion beam analysis in general.

3.1 ION BEAM ANALYSIS (IBA)

Ion beam analysis is a cluster of techniques [41], which are based on interactions between the energetic ions and the bombarded material. Most of the interactions are between the projectile ion and the component atoms or ions of the materials. The different interactions between the charged particles of the ion beam and the target material can be seen in figure 3.1.

In these interactions, the projectile (incident) ions penetrate the solid material, loses energy along the path. The energy-loss mechanisms are governed by the incident beam energy, the atomic number of the incident ion and the atomic number of the target material. The underlying coulomb interaction between the target atoms or ions and the incident ions as they penetrate the solid, results in energy loss due to the nuclear stopping or electronic stopping. Nuclear stopping involves the energy loss due to the interaction between the incident ions and nuclei of the target atoms. This collision (star-like blast in figure 3.1) involves large discrete of energy loss and high angular deflection of the trajectory. Electronic stopping is due to the collision of the incident ion and the electrons of the target atoms. The energy losses in this interaction are much smaller with negligible lattice disorder [42]. All these interactions result in emission of particles or radiation whose energy is characteristic of the elements, which constitute the sample material.

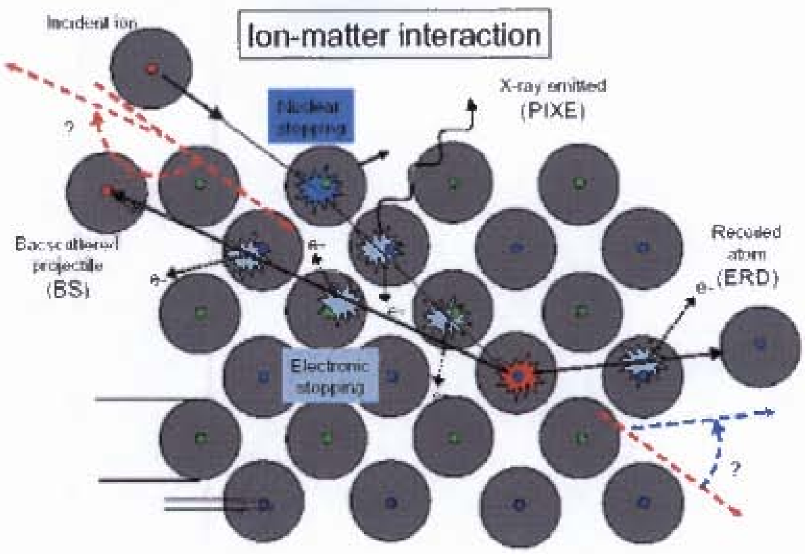

Figure 3.1: Principle of ion- solid interactions inside the target material [43].

Figure 3.2 indicates the various techniques of ion beam analyses that are used for determining depth profiling, elemental composition and concentration, thickness of thin films, and structural information.

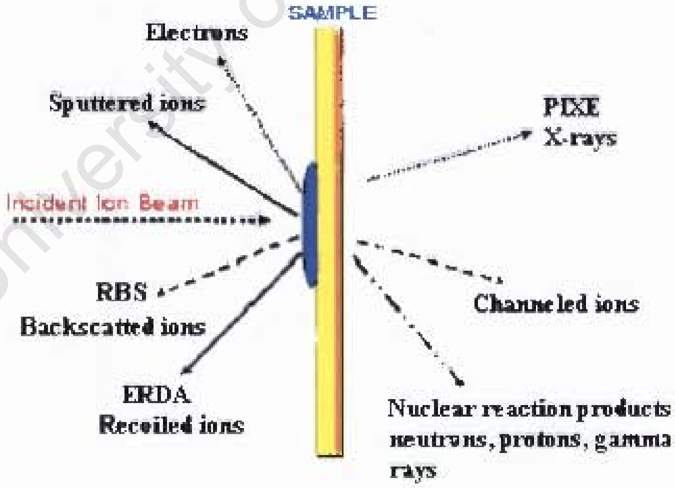

Figure 3.2 showing the various techniques in Ion beam analysis [44].

3.1.1 PARTICLE INDUCED X-RAY EMISSION (PIXE)

Particle induced x-ray emission basically involves the bombardment of the incident ions on a target material, which results in the ionization of the inner shell atoms, thus producing a vacancies that is filled by outer shell electrons. The drop down of electron results in the emission of a characteristic energy of the element under investigation. The x-rays and intensities are converted to elemental concentrations [45].

3.1.2 CHANNELING

Channeling involves the alignment of the ion beam with the crystallographic axes or planes of the sample providing information about the crystalline quality of the material [46]. Consider for example, a target material with the axis of its lattice is align parallel to the incident ion beam. The particles backscatter from the near surface region (first few monolayer) of the material are of the same yield with non-align sample, but the yield tends to drastically reduce as the incident beam goes deeper into the material because the atoms deeper in the sample were shielded away from the incident beam by the atoms in the surface region. However, if there are defects, disorder or impurities in the lattice of the target the yield increases.

3.1.3 SECONDARY ION EMISSION

This is an emission that results due to interaction between a target material and charged particles of heavier mass and of low energy, between 0.5 – 20 KeV on the surface or near the surface region. When the charged incident beam is focussed on a sample surface, there is generation of craters on the surface, a process referred to as sputtering. In secondary ion mass spectroscopy, a fraction of the sputtered atom is ionised and the resulting secondary ions are pass through separation and detection units, which are subsequently converted to concentration of the desired elements. The analysis of the remaining surface also provides information about composition and the depth profile [45].

3.2 RUTHERFORD BACKSCATTERING SPECTROMETRY

Rutherford backscattering spectrometry is one of the most powerful of the ion beam analysis techniques, and generally involves the use of helium ions (He^+) of a energy in the range 0.5 – 3.0 MeV. The specific feature of this technique is that the incoming charged particles are backscattered from the atoms in the near – surface region of the sample under investigation. This is shown in ion –matter interactions in figure 3.1. RBS allows determination of the elemental composition, impurity distribution, and its depth profiling and areal density. However, the technique can also be performed at much lower (down to 1 KeV), and also much higher energies, and is not restricted to He-ions.

This spectrometry technique has been adopted for the analysis of electronic device materials such as semiconductors, and also in the investigation of ion implantation in solid materials [47]. A tremendous amount of work has been done with the RBS technique, on the characterization of surface and near surface regions and of thin films up to a thickness of about 1μm. Most of the characterizations based on this technique are laboratory research based [48]. However, the main drawback is its inability to detect light elements, like oxygen, nitrogen and carbon in heavier substrate materials. The combination of RBS with other ion beam analysis methods allows in the thorough understanding of the material undergoing analysis. For instance, Karl et al. [49], have shown how combination with SIMS techniques could be used to obtained stoichiometric and absolute atomic concentration of buried layers. Another complementary technique with RBS is channelling, which provides additional information about local structure in crystalline systems. Also in the work, RBS is combined with ERDA and resonance scattering to provide a full characterisation of light elemental impurities.

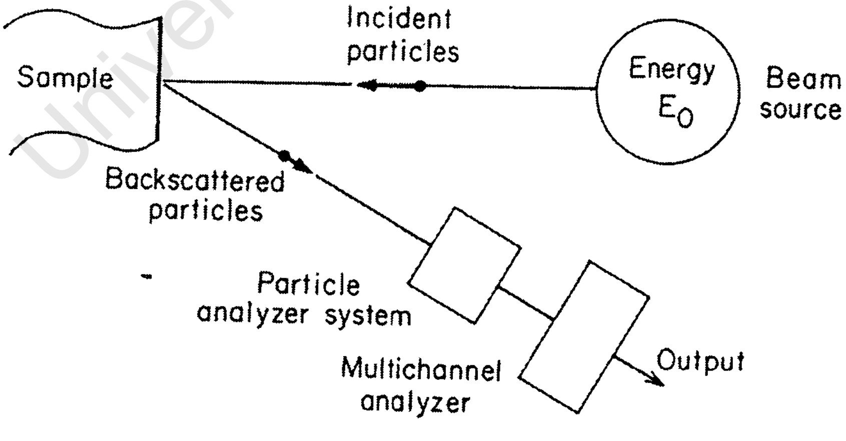

Figure3.3: Schematics of backscattering spectrometry [50].

The Figure 3.3 shows the principle of the backscattering spectrometry. An energetic helium ion (He^+) beam is impinged on a sample to be analysed. Some of the particles are backscattered and detected, generally at a fixed angle by energy sensitive analysis system.

3.2.1 FUNDAMENTALS OF BACKSCATTERING

The elastic collision between the beam ions causes some of the He^+, and ion of the target material to be backscattered. The particles are backscattered at a specific angle, as shown in figure 3.1 and with an energy characteristic of the mass of the ions of the target material. This occurrence leads to a scattering cross section σ, which tells how strong the scattering is, and from which the atomic composition can be determined as discussed in section 3.2.2. Furthermore, during the process the incident ions lose energy when traversing the material, which leads to deceleration of the ions before and after collision. The deceleration of ions in the target material is described as the stopping cross section, which enables the determination of the elemental depth distribution.

The kinematic factor K is given as the ratio of the incident energy after an elastic collision to that before the collision. It can also be explained in terms of application of conservation of energy and momentum of a two-body collision [46, 50].
Figure 3.4 shows the backscattering of ions at a depth x in a given target material, the energy of these ions detected through a differential solid angle $d\Omega$ depends on transfer of momentum during the interaction and energy-loss mechanism as seen in figure 3.1, when transversing this material.

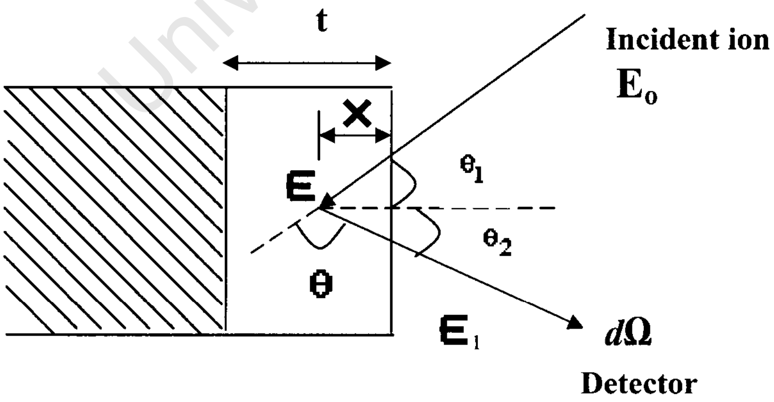

Figure3.4: Experimental geometry of backscattering spectrometry [50].

For scattering that occurred at the surface of the sample, the only energy loss is due to the momentum-transferred to the atoms of the target material and the kinematics factor is given as:

$$K = \frac{E_1}{E_0} = \left[\frac{(1 - \left[\frac{M_1}{M_2}\right]^2 \sin^2\theta)^{\frac{1}{2}} + \frac{M_1}{M_2}\cos\theta}{1 + \left[\frac{M_1}{M_2}\right]} \right]^2 , \qquad 3.10$$

Where M_1 is the mass of the incident particle, M_2 is the mass of the target atom and θ_1 *and* θ_2 are defined as the angle between the incident ion before and after scattering. θ is the laboratory angle through which the incident ion are backscattered. The kinematics factor is a function of M_1, M_2 and θ only.

3.2.2 SCATTERING CROSS SECTION

The scattering cross section, denoted as $\sigma\ (\theta)$, *is* usually expressed in terms of a differential cross section $d\sigma/d\Omega$, which is defined as the relative number of backscattered atoms into a solid angle $d\Omega$ for a given flux of incident particles [50]. As seen in figure. 3.5, a beam of incident ions is impinged on a target material of a uniform thickness and wider than the beam area. Q is the number of the ions that is projected on the material at an angle θ, if *d*Q is detected by the differential solid angle *d*Ω, then the scattering event from the target material through the solid angle is given by:

$$\frac{d\sigma(\theta)}{d\Omega} = \left(\frac{1}{Nt}\right)\left[\left[\left({}^{dQ}\!/_{d\Omega}\right)\Big/_{Q}\right]\right] \qquad 3.11$$

Where N is the volume density, t is the thickness of the depth probed, and Nt is the areal density.

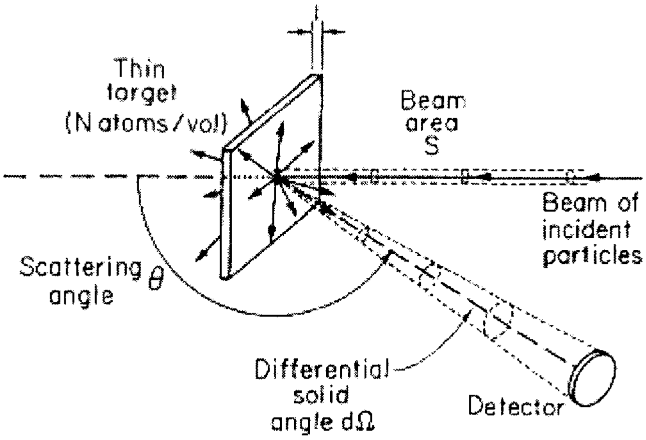

Figure3.5: Schematics of differential cross section. The backscattered particles into solid angle detector from an incident beam of area S impinge on a portion of the target material [50].

For an elastic collision, the differential cross section is calculated by introducing the principle of the conservation of energy and momentum together with the coulomb repulsion forces of the two nuclei, which gives:

$$\frac{d\sigma}{d\Omega}=\left(\frac{Z_1Z_2e^2}{4E}\right)^2\frac{4\left[\left((1-\left\{\frac{M_1}{M_2}\right\}\sin\theta)^2\right)^{\frac{1}{2}}+\cos\theta\right]^2}{\sin^4\theta\left[1-\left(\left(\frac{M_1}{M_2}\right)\sin\theta\right)^2\right]^{\frac{1}{2}}} \qquad 3.12$$

Where Z_1 is the atomic number of the incident ion with mass M_1, Z_2 is for the target atom with mass M_2, E is the energy of the incident beam before scattering and e is the electronic charge.

The differential cross section depends only on the ratio of M_1/M_2 of the incident and target masses and on the scattering angle θ. At $\theta = 180$, scattering angle is at miximum. For $M_1 << M_2$, a simple rule of thumb is applicable for the scattering cross section which is proportional to the square of atomic number Z of the target material, and can be expressed as:

$$\sigma \propto \left[\frac{Z_1Z_2}{E}\right]^2 \qquad 3.13$$

During a scattering event, the probability that the number of atoms 'seen' by a very small detector solid angle Ω rather than differential solid angle $d\Omega$, for a well defined scattering angle θ, is described by average differential scattering cross,

$$\sigma \equiv \frac{1}{\Omega}\int_{\Omega}\left[\frac{d\sigma}{d\Omega}\right]d\Omega \qquad 3.17$$

Experimentally, as shown in figure 3.5, for a uniform beam projected on a uniform target material of wider area than the beam will backscatter a total number of detected particle A, which corresponds to the concentration or the yield per unit area

$$A = \sigma[\Omega]\times\Omega\times Q\times(Nt) \qquad 3.18$$

Number of Detected particles = σΩ X Total Number of Incident particle X Number of atom per unit area

Where (Nt) is the areal density, Q is the number of incident ions, Ω is the subtended solid angle and $\sigma[\theta]$ is the scattering cross section. Also, the number of impurities per square centimetre can be determined from the area of the signal A, given by the total number of the counts integrated over the region of interest, which is seen in section 3.2.5

3.2.3 ELEMENTAL SENSITIVITY

Rutherford backscattering is more sensitive to elements with higher atomic number due to their large nuclei. The sensitivity to heavy elements resulted from the dependence of the cross section on Z_2^2. However, as seen in figure 3.6, the energy separation between the backscattered particle from light elements are greater than that of the heavy elements, which is due to the momentum transferred from the incident particle to a light atom. As the mass of the target atom increases less momentum is transferred. This then means that momentum transfer determines the mass resolution, which is good for light elements and poor for the heavy elements [46]. For instance, in a material, the yield from the same ratio composition of elements differ due to their different masses which resulted from different cross section, with significant yield from element of heavier mass. This therefore implies that there is better detection and accuracy for elements with heavier mass in a material. The yield ratio of the sample of the two elements is thus, given as the ratio of the scattering cross section of these elements proportional to the square of the ratio of the atomic number Z_H and Z_L of the heavy and light elements respectively, a factor contributing to sensitivity of heavier element.

$$\frac{\sigma_H}{\sigma_L} = \left(\frac{Z_H}{Z_L}\right)^2 \qquad 3.14$$

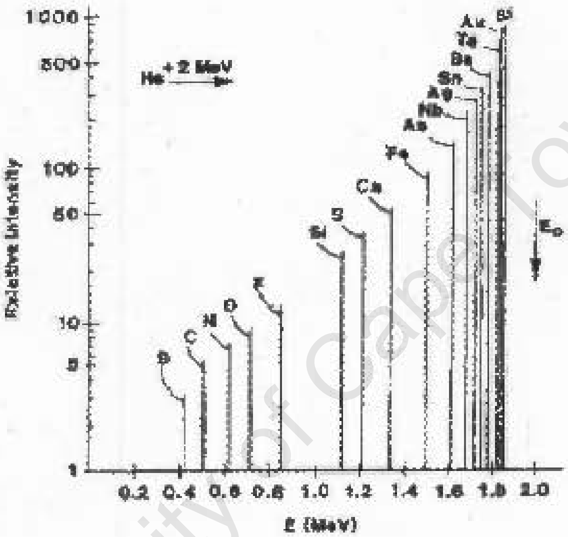

Figure3.6: He^+ Backscattering yields from some selected elements. Elements with higher atomic number or heavier mass are more sensitive [46].

3.2.4 ENERGY LOSS AND STOPPING CROSS SECTION

The energy loss, denoted by dE/dx, mechanism may be due to electronic or nuclear stopping in a target material as previously seen in figure 3.1. This is due to the interaction of the incident beam with the atom of the target material when traversing such a sample. The interaction results in slowing down of incident beam ions, which mean that the incident particle loses energy in the inward path, and again on the outward path.

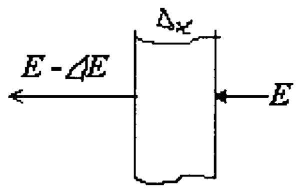

Figure3.7: schematic diagram of energy loss in a material medium, where the incident loses energy ΔE while traversing distance Δx

The calculation of the energy loss, ΔE, of ions traversing a target material is often involve the integration of the stopping power as in

$$\Delta E = \int \frac{dE}{dx} dx \cdot \qquad 3.15$$

The energy loss per distance travelled in the material is a function of velocity of the incident beam, material composition and density. When incident beam is perpendicular to the target, an area S is illuminated by the incident beam, N is the atomic density, SN is the contribution of the atoms in the area and Δx is the thickness as seen in figure 3.7. The surface density of the atoms is given as:

$$\frac{SN\Delta x}{S} = N\Delta x$$

This quantity increases linearly with Δx. If incident beam is at angle θ to target, area illuminated in $S/\cos\vartheta$

Thus, $$\Delta E = \left(dE/dx\right)\Delta x$$

Therefore, ΔE is set such that is proportional to NΔx.

The proportionality factor is referred to as stopping cross section [ε].

Stopping cross section is thus defined as the independent contribution of individual atoms in a target material expressed as the average over possible energy-dissipated process initiated by the incident beam on its path in the material [50].

Thus,

$$[\varepsilon] = \left[\frac{1}{N}\right]\frac{dE}{dx} \qquad 3.16$$

Where [ϵ] = stopping cross section.

3.2.5 DEPTH PROFILING

The concentration depth profile for a particular impurity is determined from its contribution to the backscattered particles as a function of energy. This depends on:

i) the Kinematic factor,
ii) energy loss when traversing on the way into a certain depth, and
iii) energy loss on the way out from this depth.

As previously described in figure 3.1, as the incident beam transverses the target material, the energy-loss mechanism, results in the determination of material composition and the depth distribution of the element in the target material. The two energy –loss mechanism depends on the beam energy E_o and the atomic number of incident ion Z_1. The nuclear stopping is pronounced when E_o is low and Z_1 is high while energy loss is due to electronic stopping if E_o is high and low Z_1 [42].

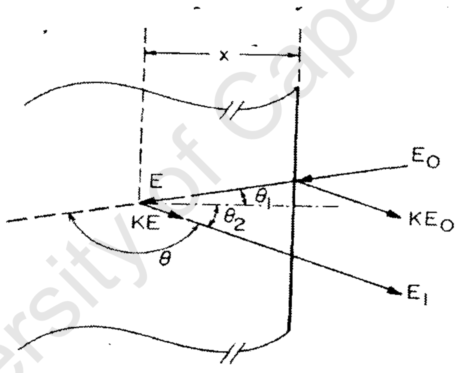

Figure3.8: schematics representation of the depth reached by an ion beam with incident beam energy E_o, backscattered through an angle with a final energy E_1, $\theta_1+\theta_2+\theta=180^o$. KE_O is the energy of particles backscattered at the surface of the sample[50].

Figure 3.8 illustrates the depth reached by an incident beam with energy E_o. Assuming the energy loss is constant along the path in and out of the target material, then as the ion transverses the material, the energy loss along the path into the material is given by:

Energy loss inwardly = $E_{in} = E_o - \frac{x}{\cos\theta_1}\left.\frac{dE}{dx}\right|_{E_o}$ 3.19

The energy E_x immediately before scattering at the depth x is given as:

Energy before scattering at depth X = $E_o - E_{in}$ 3.20

And the energy after scattering is:

Energy after scattering = $(E_o - E_{in}) \times K$ 3.21

Since *dE*/*d*x is assumed to be constant, the energy loss on the outward path is given as:

Energy loss outwardly =

$$E_{out} = KE - \left.\frac{dE}{dx}\right|_{E_1} \times \frac{x}{\cos\theta_2} \qquad 3.22$$

The subscript E_0 and E_1 refer to constant d*E/dx* along the paths; KE is the energy backscattered from the surface of the material.

$$E_1 = E_{in} - E_{out}$$

E_1 is the measured energy of particle backscattered from depth x in the material. Then ΔE, is the energy difference between E_1 and KE_0, which is written as:

$$\Delta E = KE - E_1 = \left[\frac{K}{\cos\theta_1}\left.\frac{dE}{dx}\right|_{in} + \left.\frac{dE}{dx}\right|_{out}\frac{x}{\cos\theta_2}\right] \qquad 3.23$$

And equation 3.23 can be written as:

$$\Delta E = [S]x \qquad 3.24$$

Where

$$[S] = \left[\frac{K}{\cos\theta_1}\left.\frac{dE}{dx}\right|_{in} + \left.\frac{dE}{dx}\right|_{out}\frac{1}{\cos\theta_2}\right]$$

[S] is define as the energy loss factor.

More over, a similar expression can be written in terms of the stopping cross section instead of energy loss:

$$\Delta E = [\varepsilon]Nx$$

Where, N is the atomic density and

$$[\varepsilon] = \left[\frac{K}{\cos\theta_1}\varepsilon_{in} + \frac{1}{\cos\theta_2}\varepsilon_{out}\right]$$

The stopping power of a material containing < 1 % atomic concentration of impurity is determined by that of the host material and if the impurity exceed 1%, a weighted average for all the component material is used [45].

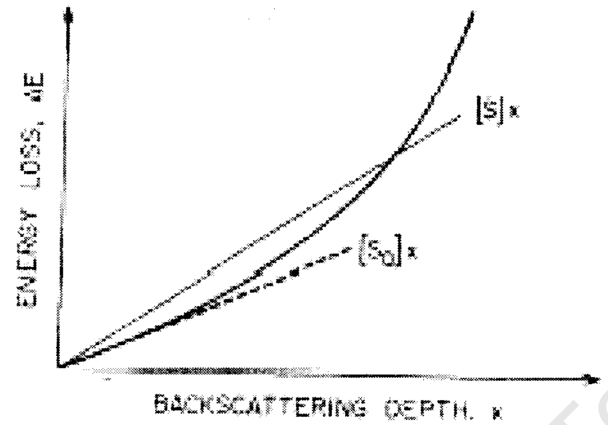

Figure 3.9: Describes graphically the linear relationship between the exact depths along the path at which scattering occurred and the corresponding energy loss factor, the curve represent the general relation between the ∂E/∂x and the depth at which scattering occurs. [S_o] symbolises the surface energy approximation which provide the linearization [50].

3.2.6 RBS SPECTRUM

For backscattering spectrum analysis, the masses of the elements and their atomic number are highly important. In a target material or sample with any surface impurities with atomic masses greater than the host element are visible in the spectrum. For instance figure 3.10 shows a typical RBS spectrum of a carbon substrate (target) consisting of oxygen, silicon and gold as surface impurities. The spectrum was simulated for 2.0 MeV He^+ backscattered at an angle of $\theta = 170^o$, solid angle of 4.11msr and a collected charge of 10 μC. The crosses indicate the channel number of the impurities and on the right–hand side of the spectrum gives the kinematics factor for the scattered elements an ideal procedure for the calibration of the system which is discussed later in chapter 4.

As discussed in section 3.2.3 and seen in figure 3.9, the cross section is proportional to the masses of the element, which in turn result in the elemental yields, thus, in the interpretation of the spectrum two basic principles are followed:

- Atomic number: high atomic number gives high yields.

- Heavy elements are at high energies: elements with heavier masses together with the kinematic factor determine the leading edge of the signal of the element.

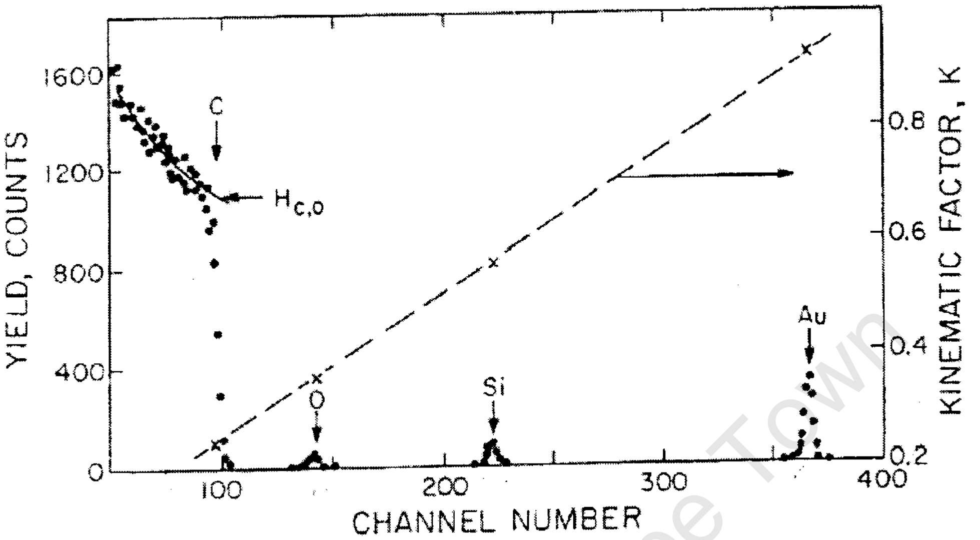

Figure.3.10; Spectrum of 2.0 MeV He+ impinged on carbon substrate containing elemental current impurities, the backscattered particles are at angle of 170° and the beam for total number of particle counted (6.25x 10^{13} ions) is 15 nA [50].

3.3 ELASTIC RECOIL DETECTION ANALYSIS

In this technique, an incident particle of mass M_1, atomic number Z_1 (often greater than the target atom) and energy E_o as seen in figure 3.11, is directed at a glancing angle on to a target atom of mass M_2 and atomic mass Z_2, resulting in a binary collision. Atoms ejected as result of these interactions are scattered in a forward direction (recoiled), passing through a thin filter (typically, Mylar of thickness ≈12.5 μm) that is placed in the detector system, to stop and block-out the elastically scattered particles and allow the passage of lighter atoms. Doyle et. al. [51] demonstrated the use of alpha particles (He^+) for depth profiling of hydrogen and its isotopes. In this case, the helium ion which is heavier than hydrogen is blocked out by the mylar foil, while hydrogen passes through due to its low stopping power compared to He. [38].

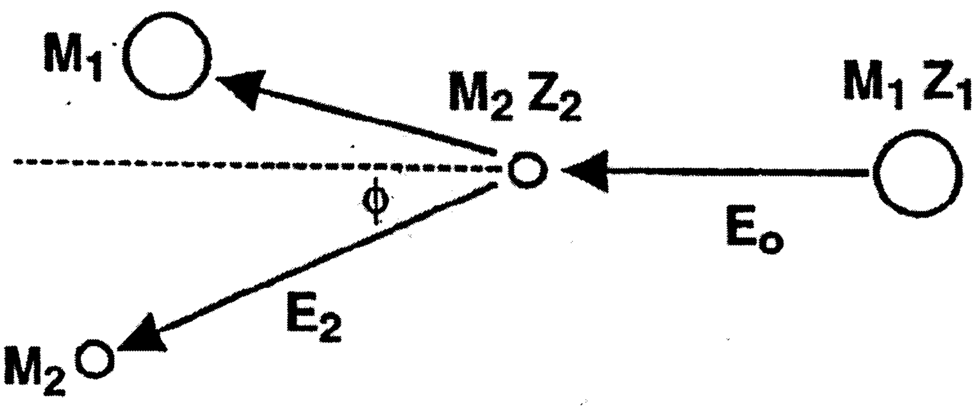

Figure3.11 kinematics of ERDA as seen the laboratory frame of reference [52].

Elastic recoil detection analysis (ERDA) is also a complimentary technique to Rutherford backscattering- its physical concept and experimental setup are almost the same. Basically, in the Rutherford backscattering technique atoms are scattered backwardly while in the target atoms are recoiled and detected in ERDA. Information about the sample material can be acquired using both techniques simultaneously in a single run. The information obtained can be analysed using the computer program (RUMP) [53] to achieve full a quantitative study. The RUMP program does the calculation based on simulation and fitting the composition of the sample, taking into consideration the energy loss, detector resolution and straggling effect.

Tremendous work has been done in many areas in improving the technique, a few of which are listed below:

(i) Sensitivity: Avasthi et al. [54] demonstrated the use of two dimensional position sensitive detectors in studying the electronic excitation induced damage in single crystal.

(ii) Depth resolution: Siegele et al. [55], reported the application of micro beam heavy ion ERDA using a large solid angle ΔE – E telescope to layered structures.

(iii) Characterization: Udhajasaikan et al. [56] characterized as-grown and ion implanted GaAs crystal, detecting and quantifying hydrogen and Waijers et al. [57] reported the application of the technique to characterise silicon rich silica, containing silicon nanocrystals produced by nucleation and growth of radicals.

3.3.1 FUNDAMENTALS OF ERDA

This technique depends on only four physical concepts:

- The Kinematic factor
- Differential cross section
- Stopping power
- Energy straggling.

Kinematics

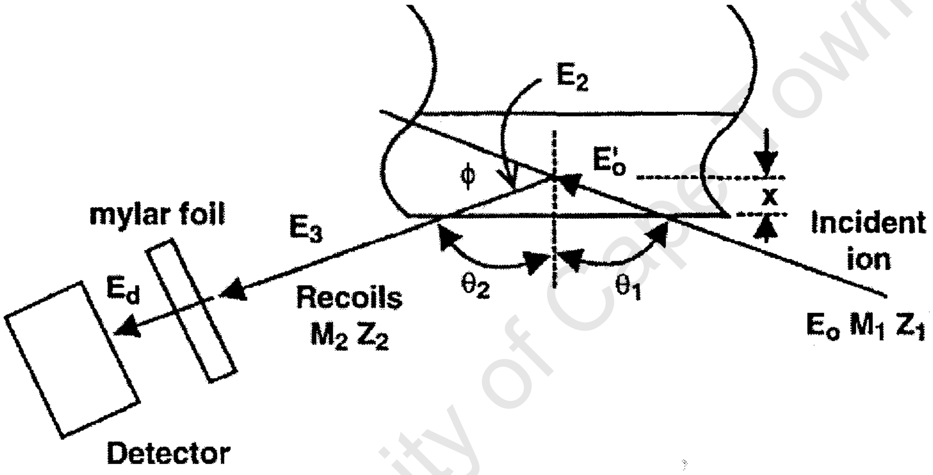

Figure 3.12: Schematic diagram of experimental setup of ERD, showing the geometry of the incident ion and recoiled particle [52].

Figure 3.12 shows the laboratory frame of reference in which an incident of beam energy of E_o, mass M_1 and atomic number Z_1 being impinges on a target material at an angle θ_1. The recoiled atom is forward scattered at angleϕ. Such that

$$\theta_1 + \theta_2 + \phi = 180^o \ . \qquad 3.25$$

if $E_o - E_o^1$ is the energy loss by incident beam when penetrating a depth x, before the recoiling off the atom of mass M_2, with atomic number Z_2, the energy of the recoiled atom E_2 scattered at an angle ϕ, can be related to the incident energy E_o by the kinematic factor.

$$E_2 = KE_o \ . \qquad 3.26$$

The kinematic factor is

$$K = \frac{4M_1M_2\cos^2\phi}{(M_1+M_2)^2} \quad . \qquad 3.27$$

Therefore, as seen in figure 3.11, the initial energy of the recoiled atom can also be estimated by

$$E_2 = KE_o^1 \ . \qquad 3.28$$

After traversing the sample, the recoiled atoms emerges with energy E_3 from the material, which is further reduced to E_d due to passage through filter.

3.3.2 SCATTERING CROSS SECTION AND QUANTIFICATION

The scattering cross section is governed by the coulombic scattering model [58] and can be expressed for elastic collision (Rutherford) in the laboratory reference frame as

$$\frac{d\sigma}{d\Omega} = \frac{\left[Z_1Z_2e^2(M_1+M_2)\right]^2}{4E_o^1M_2^2\cos^3\phi} \quad . \qquad 3.29$$

Z_1, Z_2 and M_1, M_2 are atomic numbers and masses of the incident and the recoiled ions respectively, ϕ is the recoiled angle and e is the electronic charge.

As discussed earlier in section 3.2.2, in determining or quantifying the concentration of sample atoms or impurity atoms in a given material, the following experimental parameters must also be considered: the detector subtended angle Ω, number of incident particles n_p, the tilt angle ϕ, and the yield of recoiled atoms R_a. Relating these, the following equation gives the concentration of the target atoms in atoms/cm^2 [54]:

$$n_r = R_a \frac{\sin\phi}{n_p.\Omega.\left(\frac{d\sigma}{d\Omega}\right)} \qquad 3.30$$

3.3.3 STOPPING POWER AND STRAGGLING

The process of ion stopping in material involves slowing down of the ion beam as it penetrates the material, which was discussed in section 3.1. The deceleration of the beam particles results in an energy spread which is referred to as straggling. It is a result of statistical fluctuations in the number of collision processes, a situation which impairs the depth and mass resolution [52]. However, with elastic recoil detection, in addition to those parameters mention for depth profiling in RBS, i.e the kinematic factor as seen in equation 3.27, this technique also depends on the energy loss on the path inward, to reach certain depth *d*, the energy loss on the path outward before the stopper and the energy loss in the foil (stopper). The final recoiled energy can be estimated by deducting the energy loss in the foil from energy recoiled from the surface of the material, which given as:

$$E_d = K\left[E_o - \left(\frac{d}{\sin\rho}\right)\left(\frac{dE}{dx}\right)_{in}\right] . \qquad 3.32$$

The energy loss outwardly is

$$E_{ds} = E_d - \left[\frac{d}{\sin(\phi-\rho)}\right]\left(\frac{dE}{dx}\right)_{out} \qquad 3.33$$

and the energy measured in the detector is

$$E_{detector} = E_{ds} - dE_{foil}(E_{ds}) . \qquad 3.34$$

E_{foil} is the energy loss in the stopper foil as shown in figure 3.13. Therefore the detected energy is a function of depth which can be deduced from equations 3.32 to 3.34.

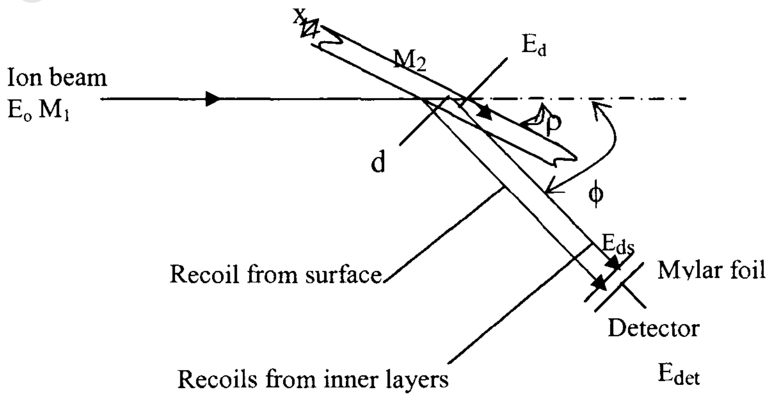

Figure 3.13: principle of depth profiling by elastic recoil detection analysis [54]

3.3.4 ERDA SPECTRUM

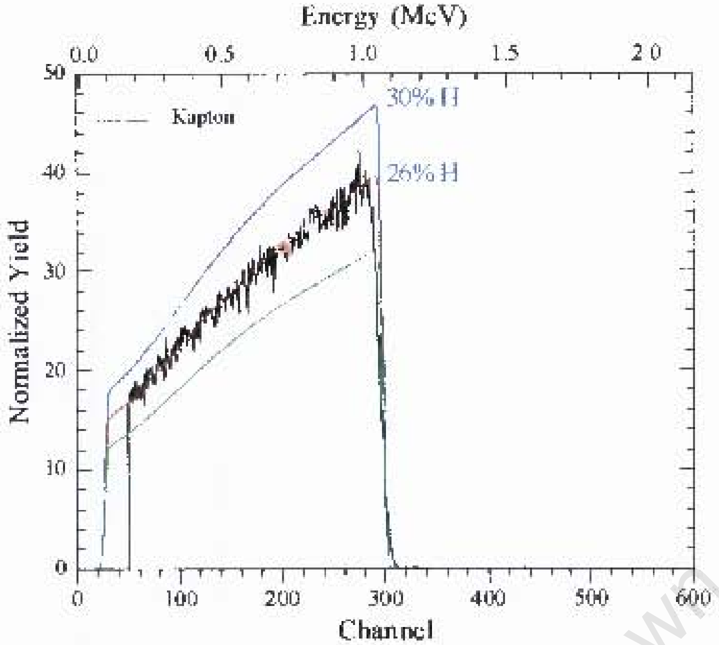

Figure.3.14. A typical ERDA spectrum showing the hydrogen content in a Kapton foil.

Figure 3.14 depicts a typical spectrum collected for kapton ($C_{22}H_{10}N_2O_4$) irradiated with beam current of 9 nA for 5 μC of charges. The spectrum was simulated for beam energy of 3.0 MeV, detector solid angle of 1.15msr and resolution of 20 KeV, at a grazing angle of 15°. The continuous red line, which fitted well (simulation) and ran through the slant edge of the lower energy channel is generated by RUMP, which gives 10 at. % of hydrogen and 26% of total composition of the compound.

3.4 RESONANCE SCATTERING SPECTROMETRY

Rutherford backscattering becomes more difficult in the analysis of trace elements or impurities of low atomic masses within substrates having high atomic masses, because the substrate tends to produce a higher yield than the impurities. The poor sensitivity for light element such as carbon, nitrogen and oxygen by RBS is overcome by the use of resonance scattering [45].

The resonance scattering technique is a subset of the Rutherford backscattering technique that utilizes high energy (greater than 3.0 MeV) to elastically backscatter from light elements or impurities independent of their matrixes. The technique is basically the same principle with RBS as only differencies in the energy variation.
Its advantages are:

- Sensitivity to low mass elements due to relative enhancement in the cross section
- Improvement in mass resolution, which increase linearly with beam energy.

This method involves varying the incident beam energy in small increments (gradually) and measuring the corresponding yield of radiation emitted due to interaction between the incident beam and impurity atoms per unit beam influence at each energy level [45].

When the resonance energy is reached at a particular depth, a nuclear reaction (narrow band) occurs (such as $^{16}O(\alpha, \alpha)O^{16}$ when probing for oxygen with He^+) at a rate proportional to the concentration of the impurity atom. Assuming the depth is x, the incident ion beam energy is E_o, resonance energy E_R and θ the scattering angle can be related according to:

$$E_o = E_R + \left[\frac{dE}{dx}\right]_{in} \frac{x}{\cos\theta} \quad . \qquad 3.35$$

This technique is normally associated with a sharp peak when the resonance energy is reached, due to the high magnitude or dramatic increase in the scattering cross section (see figure3.14). The sensitivity of this technique to light elements explains the reason for adopting it in the characterization of our samples.

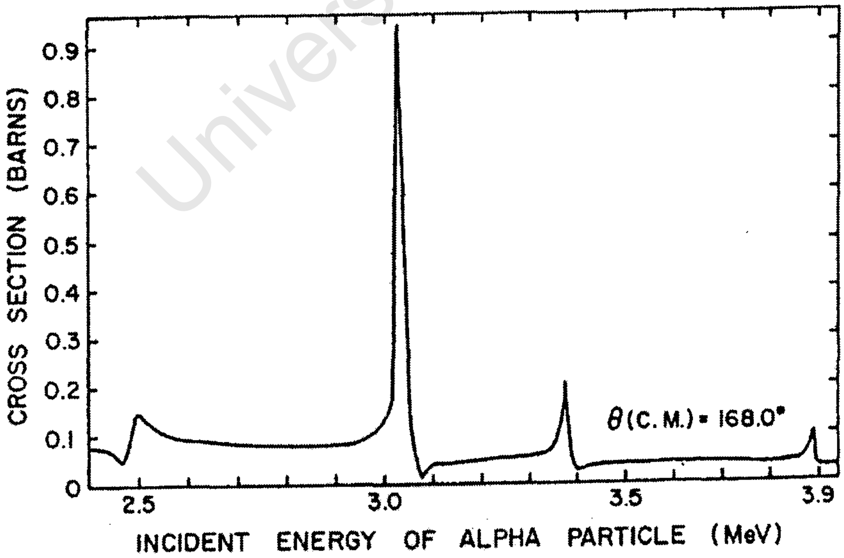

Figure 3.14 The magnitude of the cross section for helium scattering off oxygen as a function of energy [45].

3.5 Scanning Electron Microscopy.

A scanning electron microscope is an image forming laboratory analysis equipment by means of low energy electrons. It is widely used for the characterization of materials because of the high image resolution of the topography and morphology that can be obtained with great depth of field at a very low or high magnification. It involves scanning of a beam of electrons over a specimen, thus as the specimen is being bombarded with electrons, a series of interactions as shown in figure 3.15 occurs. There may be elastic reflection of electrons, or inelastic processes may result in secondary electron emission, emission of X –rays, emission of visible light (cathodoluminescence) or resulting electric charges within the specimen. The most widely use in these emissions are the secondary electrons, backscattered electron and X-rays.

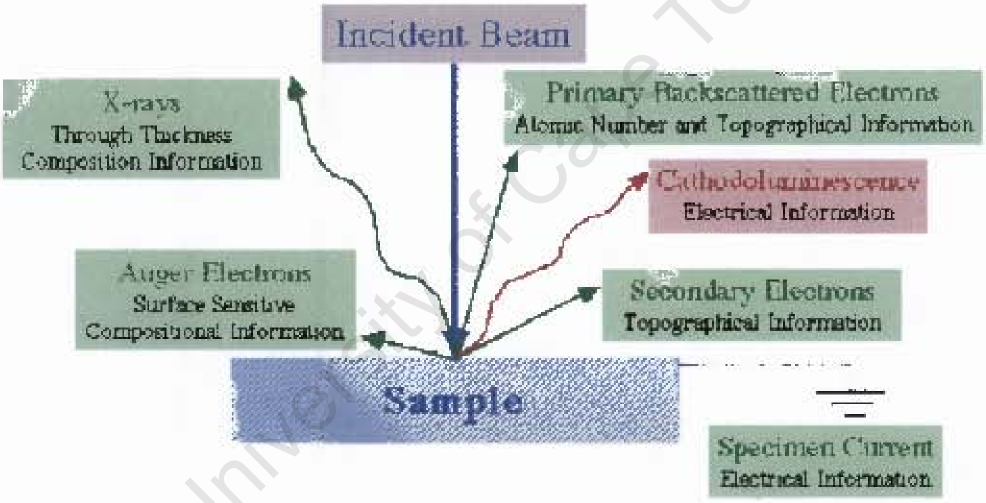

Figure 3.15: Information provided as a result of electron/specimen interactions [59]

4 EXPERIMENTAL TECHNIQUES

The deposition and characterization techniques described in the previous chapter have been used in the analysis of hydrogenated amorphous silicon (a-Si:H) and nanocrystalline silicon. The preparation and experimental setup details are described in this chapter.

4.1 Sample Preparation

4.1.1 Hydrogenated amorphous silicon (a-Si:H)

a-Si:H films were deposited by the hot wire chemical vapour deposition technique, using the MVSystem HWCVD system (see figure 4.1) at the University of Western Cape (UWC). The equipment is a single–chamber hot wire CVD deposition system that consists of two vacuum chambers: load lock and a ultrahigh vacuum chamber in this, the deposition is performed. Between the load lock and reaction chamber is a gate valve which keeps the reaction chamber pressure while operating the load lock. The substrate holder is mounted on a track in the load lock chamber.

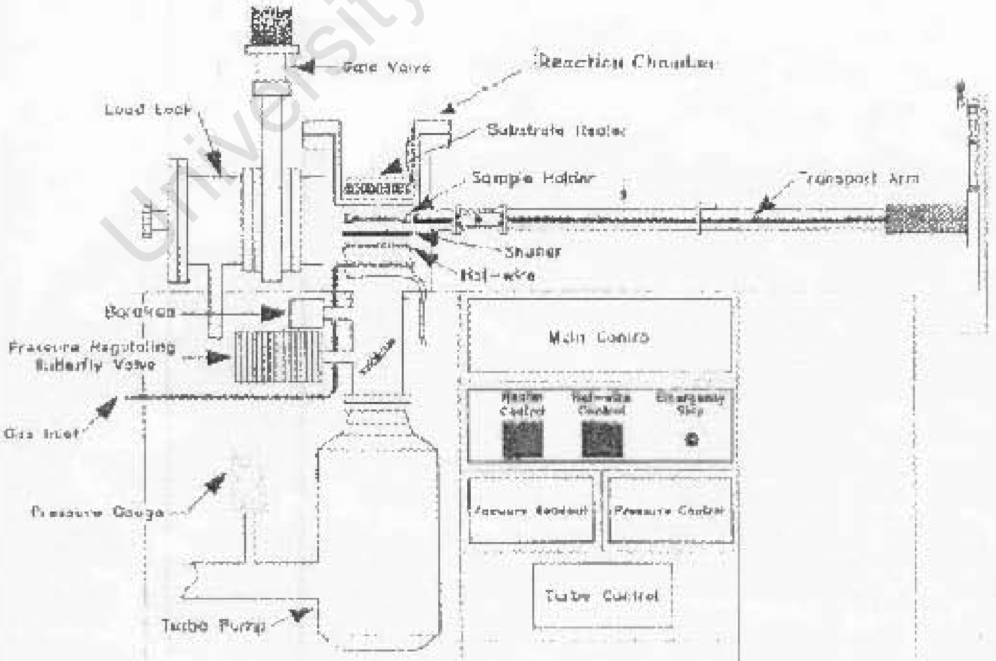

Figure 4.1: schematics of the MVSystem HWCVD reactor[60]

As substrates corning glass 7059 and silicon wafers were used. Corning glass were treated with acetone and methanol for 5 minutes to degrease the substrates. Silicon wafers were etched in 5% hydrofluoric acid (HF) to remove the thermally grown oxide. The different substrate were loaded into the substrate holder in the load-lock via the carrier track. The load lock was pumped down to a pressure of $\approx 10^{-3}$ µbar. Afterwards, the substrate holder was transported to the reaction chamber, via the transport arm, at an attained pressure of 10^{-5} µbar. Before deposition, silane gas was injected into the chamber, and the current turn on to heat the tantalum filament. The shutter was opened after equilibrium temperature of the filament was attained. The substrate temperature was controlled by an external heater but also heated due to radiation from the filament, therefore the total temperature was monitored by a type K thermocouple. The filament temperature was measured by an optical pyrometer. After deposition, the samples were cooled to room temperature with the shutter open and the filament turned off. Deposition were performed at different substrate temperatures, different gas pressure and for different deposition times as summarised in table 4.1 for different a-Si:H samples.

Table 4.1. Deposition parameters for the different a-Si:H samples

Sample	Substrate Temp (° C)	Flow rate (sccm)	Pressure (µbar)	Deposition Time (mins)
Mw 145	250	60	40	11
Mw148	300	60	40	11
Mw152	350	60	40	11
Mw150	400	60	40	11
Mw153	450	60	40	11
Mw151	500	60	40	11
Mw136	300	60	80	10
Mw139	200	60	80	20
Mw140	350	60	80	20
Mw141	400	60	80	20
Mw142	250	60	80	20
Mw127	300	60	80	20

4.1.2 Nanocrystalline Silicon Powder

In this work, intrinsic nanocrystalline silicon powder produced by silane decomposition as described earlier was studied. The preparation of the sample was achieved by compressing the powder into disc palettes. The reason for this is to produce self supporting samples that can be mounted for ion beam analysis. Two different annuli of rectangular cross section, each with internal diameter 1.63cm, with depth of 1.5mm and 2.0mm respectively were machine from a sheet of an aluminium alloy. The ring together with 0.450g powder is placed into a mortar and pestle like hardened steel container referred to as die (see figure 4.2). The disc has a tiny opening at the base. On this outlet a vacuum pump was connected, to evacuate the die during compression. The pestle was inserted into the mortal and a force of 10 tons, corresponding to a pressure of 0.5 GPa, was applied to the powder using a hydraulic press (figure 4.3). It should be mentioned that the pestle fits exactly into the mortar to produce the palette. Pressure was applied for two minutes under rough vacuum. This duration with the above specified pressure allows the powder grains to hold together and form a compact specimen for the course of the ion beam analysis. Extreme care was taken during preparation to minimize surface friction so that samples with nearly uniform density throughout were produced. A total of five samples were prepared with this method. The effective density and fill factor of the samples was computed as follows:

- Final mass of the powder in the sample is = 0.140g
- Internal Volume of cylindrical ring = 0.309cm^3
- Density = 0.140/0.309 or 0.453g/cm^3

The Fill factor (FF) is the measure of the ratio of the powder density to the pure silicon density and is given as:

FF = 0.453/2.33 or 0.1944 (19.44%)

The value of the fill factor depends on the load and the pressure applied, which makes the material more compact. The effective atomic density of the nanopowder is therefore 9.7 X 10^{21} atom/cm^3, compared to the atomic density of massive silicon which is 4.992 X 10^{22} atom/cm^3, for the above examples.

Figure 4.2 Equipment for preparation of powder ion beam analysis: (a) The ring on a mount and (b) The die's accessories with the ring for the preparation of silicon powder into palette

Figure 4.3: a typical setup of compressing machine [die]

4.2 Film Characterization

4.2.1 Experimental setup

The ion beam analysis was performed at the materials research group at iThemba LABS, Faure, South Africa, using a 5.5MV van de Graaff accelerator that produces an accelerated beam of positive ions. The accelerator is equipped with belt charging system, capable of carry 200 nA charging current to the terminal. The acceleration path is provided for by an acceleration tube which is evacuated to reduce collision with excess gas molecules in the tube. Charged particles are focused on to the sample by means of a high energy beamline using a magnetic quadrupole optics, as shown in figure 4.4. The system is computer controlled, and consists of a duoplasmatron ion source, gas bottle with He or H, a focussing/analysis magnet, five beamlines, and a high vacuum experimental chamber.

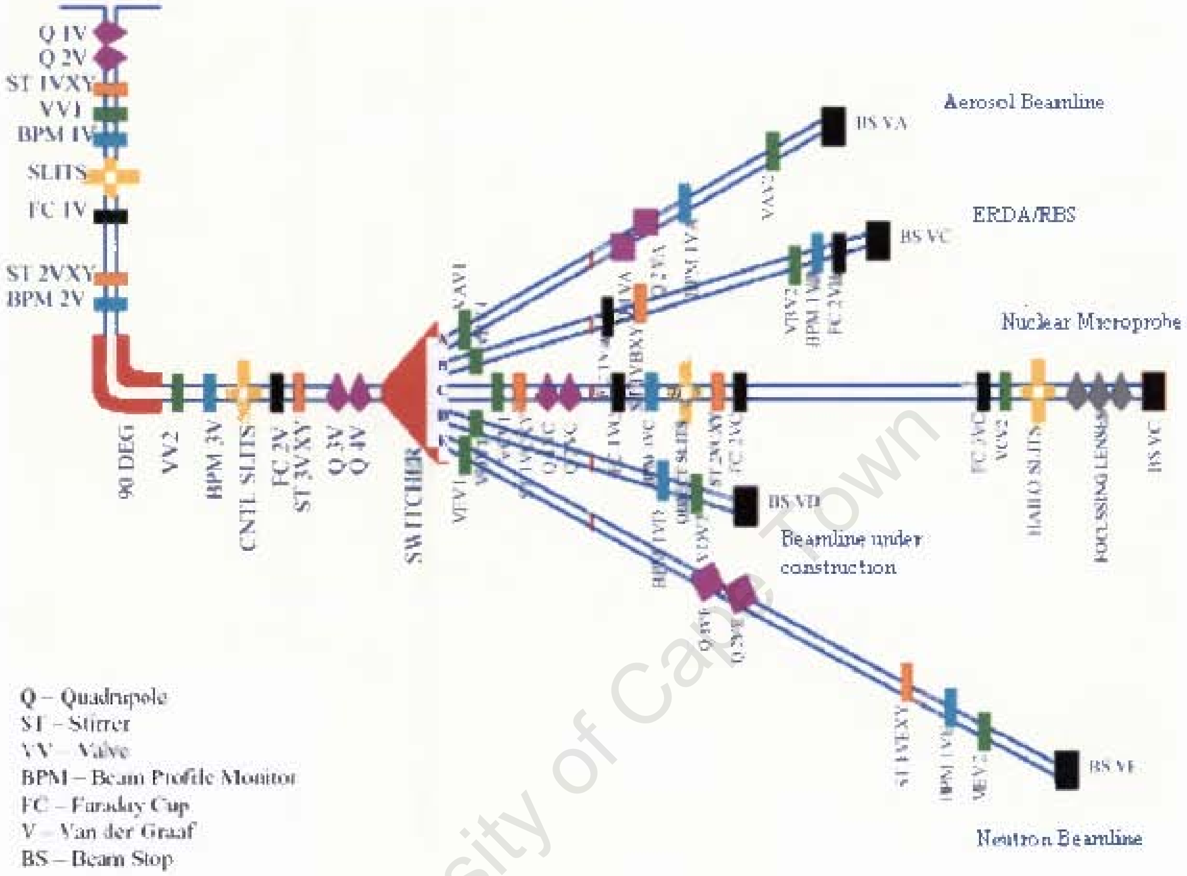

Figure 4.4: Overall layout of the accelerator, beamlines and the experimental chambers at iThemba LABS [61].

4.2.2 Beamline

The beamlines, which are five in number, are located 30° to each other providing corresponding experimental chambers for material science, nuclear, biological or environmental analysis. The beamline contains a beam collimator, which functionally defines the beam to have sharp edges and prevents scattered particles from analyzing slits entering the target chamber, is followed by two slits (X-Y) to complete the divergence of the beam. An analyzing magnet enhances the focussing capability of the beam line. Turbo molecular pumps are attached to each beamline to maintain the pressure at the required level.

4.2.3 Experimental chamber.

The experimental chamber is the final portion of the vacuum system. For the RBS and ERDA experiments, the measurements are carried out in the same chamber, which is normally maintained at a pressure of about 2×10^{-4} mBar. Figure 4.5 shows the chamber. It consist of a 14" diameter stainless steel cylinder with several ports around the circumference for analytical processing. These ports, which house the solid state surface barrier detector, are at 15° intervals. The detector is fixed to any of the ports according to the geometry of analysis to be performed. The samples were fixed on to the surface of the sample holder which is attached to a ladder that moves vertically up and down in the chamber. There is capacity for ten samples to be loaded at a time.

Figure4.5: A typical setup of RBS experimental scattering chamber at iThemba LABS

4.2.3.1 RBS/Resonance scattering

The measurements were performed in the experimental chamber with the following beam parameters and laboratory geometry: a 1-mm diameter collimated beam of He^{+} particles at 3.0 MeV. The sample holder was tilted by 10° with respect to the incident beam direction. A silicon surface barrier detector, of solid angle 1.15 msr with resolution of 20 keV, was placed at a laboratory scattering angle of 165°. The incident beam energy was changed by gradual increment of 0.02 MeV, and spectra were acquired for each energy level and analysed.

Calibration for RBS/resonance scattering

The calibration for the RBS/resonance scattering was done with standard samples (SiO_2/Si, Pt/Si, Pd/Si, Si/Si and Ti/Si). In carrying out this calibration, those samples were subjected to the same experimental conditions described above, and a beam current of 60 nA for 20 μC was used. Figure.4.6 shows the calibration spectrum for 3.0 MeV He^+ backscattered at an angle of 165°. These standard samples were made such that elements, such as Pd, Ti, Pt, and SiO_2 were deposited on silicon substrates as surface impurities. During irradiation time, silicon returns a continuous signal whose leading edge is at channel number 265. The other impurities have their peaks at channel numbers 418, 343, 449, and 152, respectively. The kinematic factor for scattering from each element is used in computing the backscattered energy, using the equation 3.10, which is plotted against the channel number. The energy per channel and offset are computed as 5.65 KeV and 288 KeV respectively, which determines the channel width of the multichannel analyzer

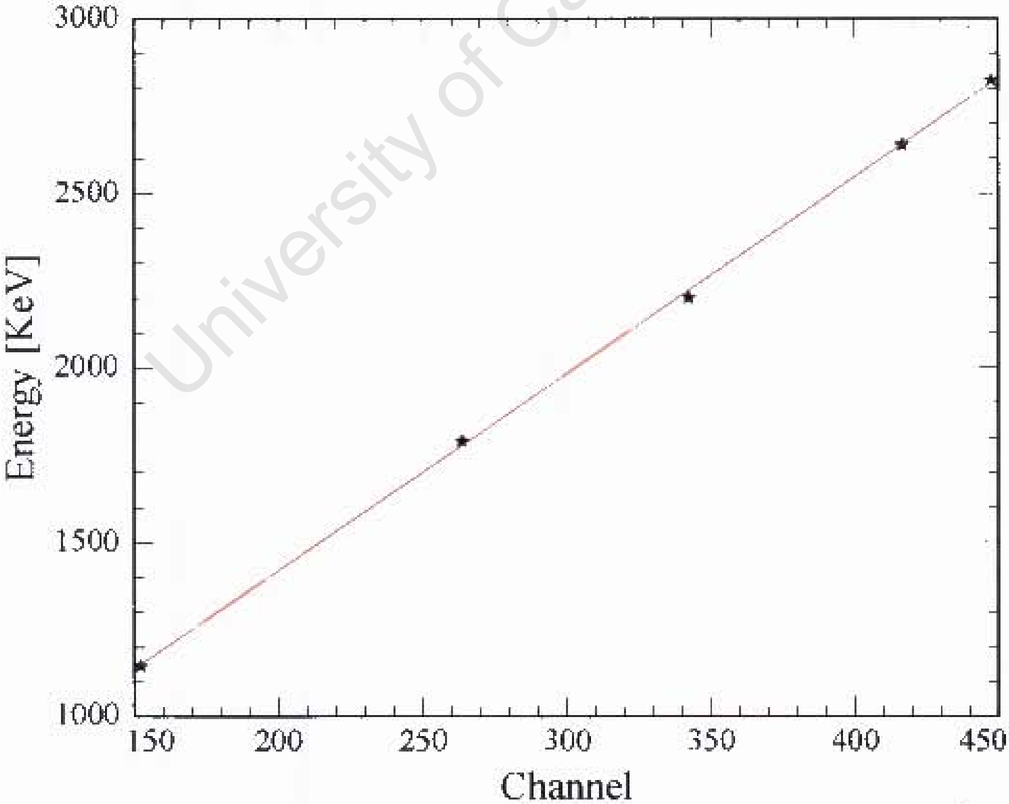

Fig. 4.6: the spectrum for 3.0 MeV calibration of He^+ backscattered at an angle of 165°

After this calibration stage, analytical measurements were preformed on samples listed in table 4.2 to 4.4 (see next page). The probing beam energy was increased from 3.0 MeV to 3.05 MeV. When operating at this high beam energy resonance scattering occurs. Resonance scattering is based on an interaction between the incident (probing) beam energy and the oxygen impurities ($^{16}O(\alpha, \alpha)O^{16}$). The elastically backscattered intensity yields a corresponding peak at this beam energy if oxygen is present in the sample, because the helium – oxygen cross section is much larger than at any other energy [52] (see figure 3.14). Further increase of the beam energy will shift the yield (peak position) to the left of spectrum. This implies that the beam loses energy as it goes deeper due to electronic stopping. At a certain depth in the sample the resonance energy is reached, as shown in figure 4.7, which results in corresponding yield and shift in the position of the peak to lower channel.

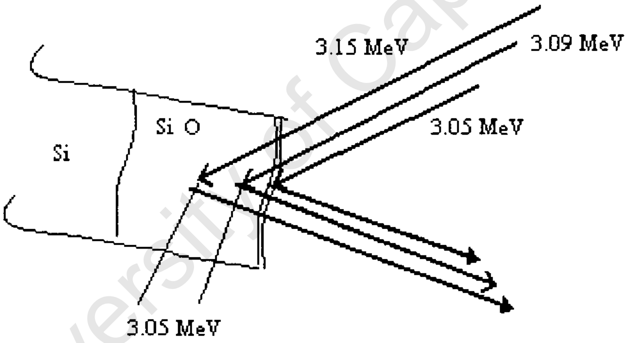

Figure 4.7: illustrates the beam energy as its traverses and reaches resonance at a certain depth in the material

Six samples (two a-Si:H and four nanosilicon powders) were investigated with this technique. For the a-Si:H, the samples analysed are labelled Mw136 and Mw 151. It is important to note, that these samples were deposited under different deposition parameters as shown in table 4.2. Sample Mw136 was deposited at a substrate temperature of 300°C and a pressure of 80 μbar while sample Mw151 was at a substrate temperature of 500°C and a pressure of 40 μbar. Table 4.3 and 4.4 shows the parameters for the other samples analysed including the nanocrystalline samples.

Samples analysed by Resonance scattering

Table 4.2: amorphous sample deposition parameters

Samples	Sub.Temp	Flow rate	Pressure
Mw151	500	60	40
Mw136	300	60	80

Table4.3: amorphous sample analysed after six months

Samples	Sub.Temp	Flow rate	Pressure
Mw151	500	60	40
Mw150	400	60	40

Table 4.4: Nanocrystalline silicon analysed

Samples immediately after prep	Sample after a week of prep.
Nc-si 1 (si0123)	Nc-si III(si0165)
Nc-si II(si0122)	Nc-si IV(si0167)

4.2.3.2 *Elastic recoil detection analysis*

As mentioned before, ERDA is setup and carried out in the same vacuum chamber but with a slightly different angular geometry. The beam of 3.00 MeV He $^{+}$ is impinged on the sample placed at a laboratory grazing angle of 15° to the incident beam. The recoiled atoms are detected at a recoiled angle of 30°. A silicon solid state detector with a mylar absorber is used. The thickness of the absorber is 12.5μm, sufficient to stop the helium ions from getting through to the detector while allowing hydrogen to pass through. The beam has a diameter of 1.54 mm on the target, and the beam current during the analysis was maintained at 20 μC for all analyses, and was monitored by a faraday cup.

Calibration for Elastic recoil detection analysis

For this setup, the calibration was achieved by using a foil of Kapton ($C_{22}H_{10}N_2O_4$) of known hydrogen concentration as reference. In this case, keeping the beam parameters and laboratory geometry constant, the foils were subjected to different beam energies of 2.0, 2.5 and 3.0 MeV. The corresponding channel number at full width half maximum (FWHM) is obtained from the acquired spectra. Using equation 3.27 with the laboratory geometry, the kinematic factor was computed. The energy loss through the Mylar foil is estimated by using Eloss computer program available at iThemba LABS or RSTOP computer program from SRIM2003 [62]. The energy measured by the detector is determined by deducting the recoiled energy from the energy loss in Mylar (see equation 3.34 and Table 4.5). Figure.4.8 shows the calibration spectrum, the energies detected are plotted against the channel number. Giving the channel width of the multichannel analyzer, thus, the energy per channel and the offset are 2.55 KeV and 19.9 KeV respectively. The same experimental procedure was followed with all the samples but at energy of 3.0 MeV

Table 4.5: Computation of the calibration parameters for ERDA

Kapton	**Channel Number**	**E_o(MeV)**	**Kinematics.F**	**E_1 (MeV)**	**E_{loss}(MeV) Mylar**	**E_{det} (MeV)**
Kapton I	422	3.0	0.480	1.440	0.341	1.099
Kapton II	308	2.5	0.480	1.200	0.404	0.796
Kapton III	170	2.0	0.480	0.960	0.507	0.453

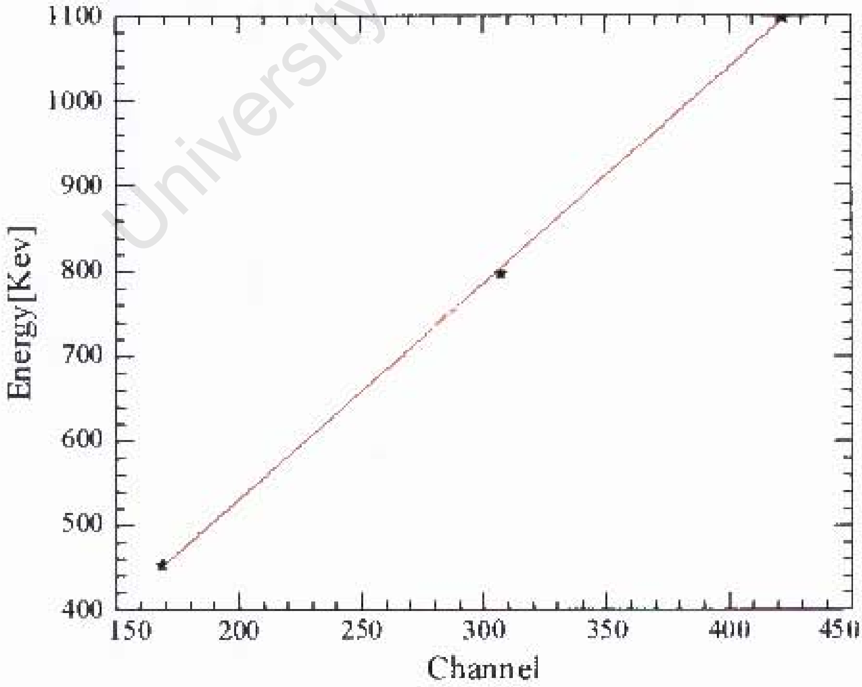

Fig. 4.8 the energy calibration of the ERDA system at 3.0 MeV of He^+ at a grazing angle of 15° and recoil angle of 30°.

Samples analysed by ERDA

After the calibration, ERDA measurements were performed on samples listed in table 4.6. The hydrogen content was determined in two phases: as-deposited and after illuminations.

Table 4.6: Sample analysed by ERDA

Samples	As-deposited	4hrs illumination	8hrs illumination
Mw136	Yes	-	-
Mw139	Yes	Yes	-
Mw140	Yes	-	-
Mw141	Yes	-	Yes
Mw145	Yes	Yes	Yes
Mw148	Yes	-	Yes
Mw150	Yes	Yes	Yes
Mw151	Yes	-	Yes
Mw152	Yes	Yes	Yes
Mw153	Yes	Yes	-

4.3 SCANNING ELECTRON MICROSCOPE

The micrograph images were taken with the Leica S440 scanning electron microscope at the University of Cape Town (figure 4.6). The S440 is an automated system that produces digital images. It uses an LaB_6 filament as the electron beam source, and has the capability of resolving images in the nanoscale range at 40 KV.

The system is also fitted with Fisons Kevex energy dispersive X-ray analysis system, and Oxford monochromator cathodoluminescence system. The micrograph images were taken in secondary electron mode at a magnification between 5000X and 15000X, and electron energies of 10 and 15 KeV and probe current of 20 pA.

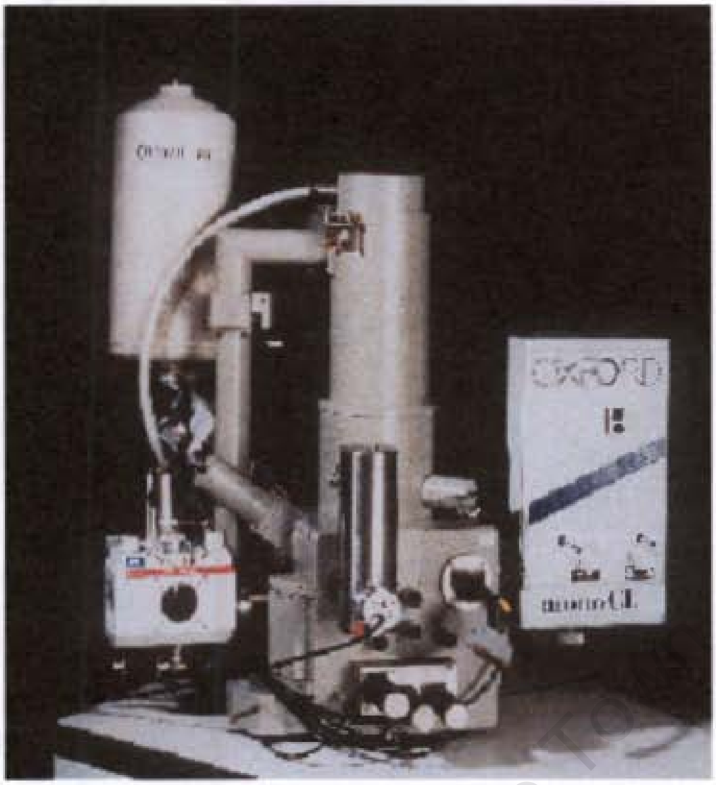

Figure 4.9 Showing the Kevex EDX system (left) and the Oxford monoCL sytem (right) [63].

5 RESULTS

The results of ion beam analytical techniques described previously on the hydrogenated amorphous silicon and nanocrystalline silicon are presented in this chapter. Subsequently, the section is divided according to each analytical technique. In section 5.1, the results of analysis obtained from RBS/Resonance scattering, are given, followed by the results of elastic recoil detection analysis in section 5.2.and Section 5 .3 covers Scanning Electron Microscopy.

5.1 RBS/Resonance scattering analysis

For samples Mw136, grown at 300°C, below the oxygen resonance of 3.05 MeV, the Rutherford backscattering spectrum is a simple step function with the leading edge signal at channel number 270 corresponding to backscattering from silicon surface as seen in figure 5.11(a). As the beam energy are gradually increased, there was an appearance of a resonance peak at the incident beam energy of 3.05 MeV, which signifies the presence of oxygen in the amorphous silicon sample (see figure 5.11(b))

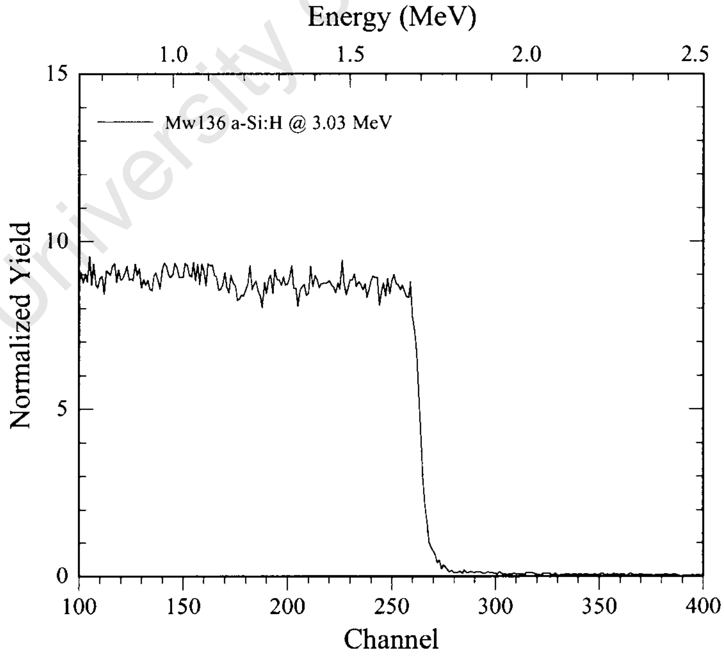

Figure 5.11(a):RBS the spectrum and simulation acquired at 3.03MeV for amorphous silicon.

The peak remains as the beam energy is increased above the resonance, indicating that, for this sample, the oxygen is distributed throughout the depth (see in figure 5.12).

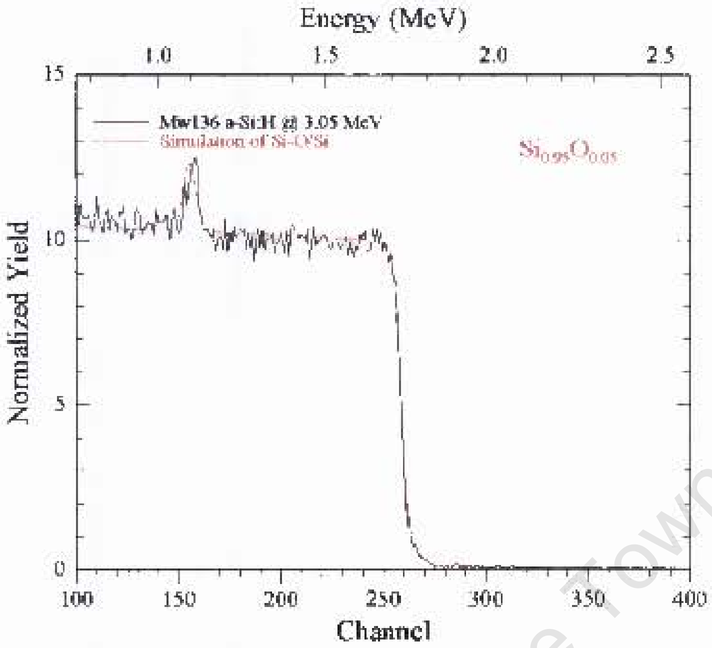

Figure 5.11 (b): RBS the spectrum and simulation acquired at 3.05 MeV for amorphous silicon.

As seen in figure 5.13, with the gradual increase of the probing energy the peak gradually shifts inward to the lower energy channel (left hand side of the spectra), which means that scattering occurs deeper in the sample material. The incident energy reduces as its traverses the material due to the energy loss, when the resonance energy is reached at a certain depth, there is an interaction between the beam and any impurity atom in the sample (oxygen in this case). The yield is proportional to the concentration of the element(s). Similarly the energy of the backscattered particle is reduced because it travels further through the material before exiting from the surface. Figure 5.13 shows the overlaid spectra with different energy beams impinged on the amorphous material and the gradual shift of the peak. There is, of course, also a systematic shift to higher energy of the silicon edge because of the higher incident beam energy.

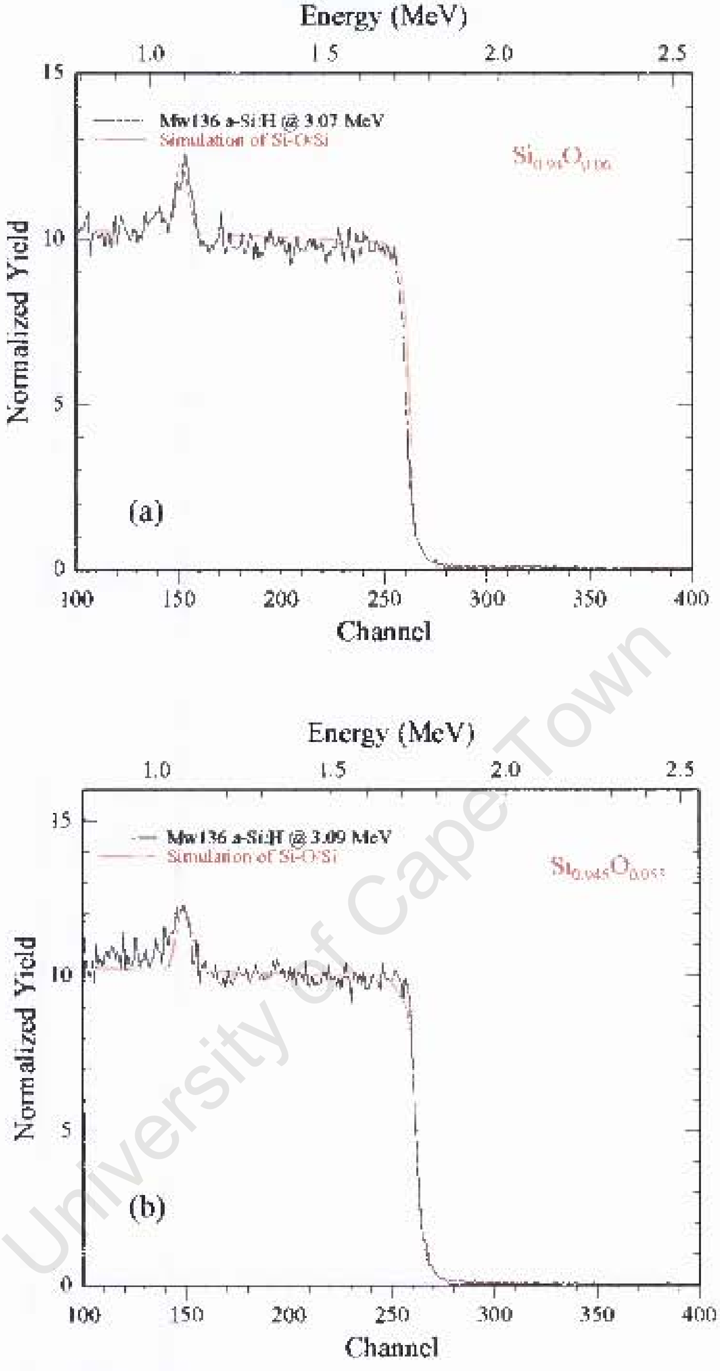

Figure.5.12: RBS spectra and simulation for sample Mw136 at energies (a) 3.07 MeV and (b) 3.09 MeV. The results show the peak to be fairly constant at these energies.

Figure 5.14(a) shows the simulated relationship between the energy and the depth which is consistent with literature [45, 50]. The RUMP simulation of these spectra reveals that the oxygen is fairly uniform in the sample, which varied between 4.5 at. % - 6.0 at. % as shown in figure 5.14(b).

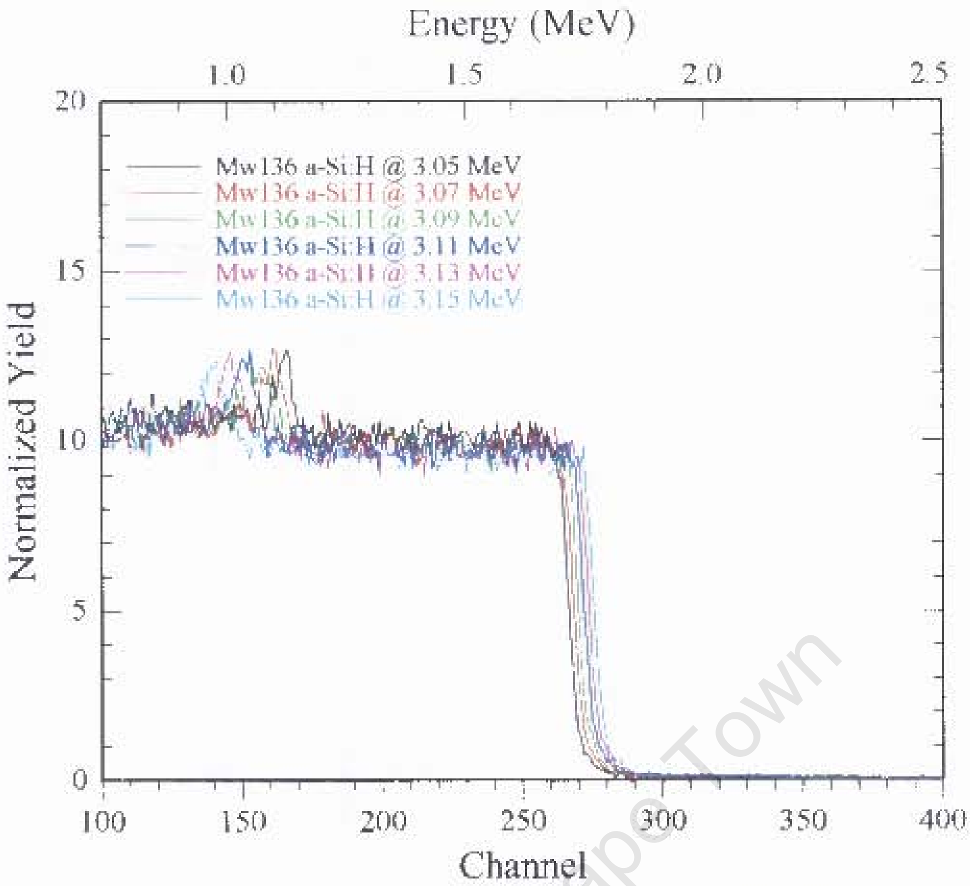

Figure 5.13 shows the spectra for Mw136 at different energies and gradual shift of the resonance peak from it original position to the lower energy channel of the spectra until it finally disappears.

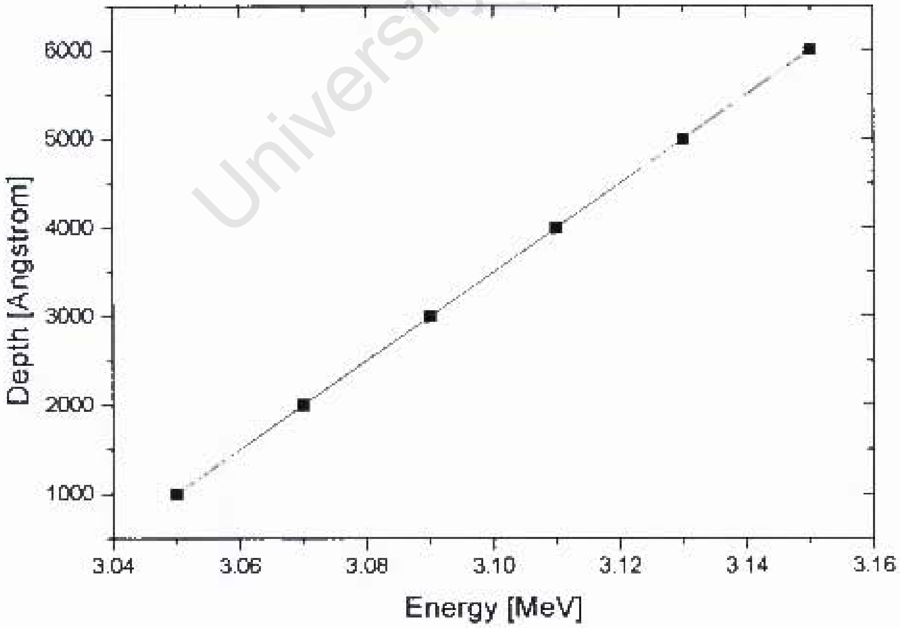

Figure 5.14(a). The general relationship between energy and depth, for the 3.05 MeV resonance peak, in the given material.

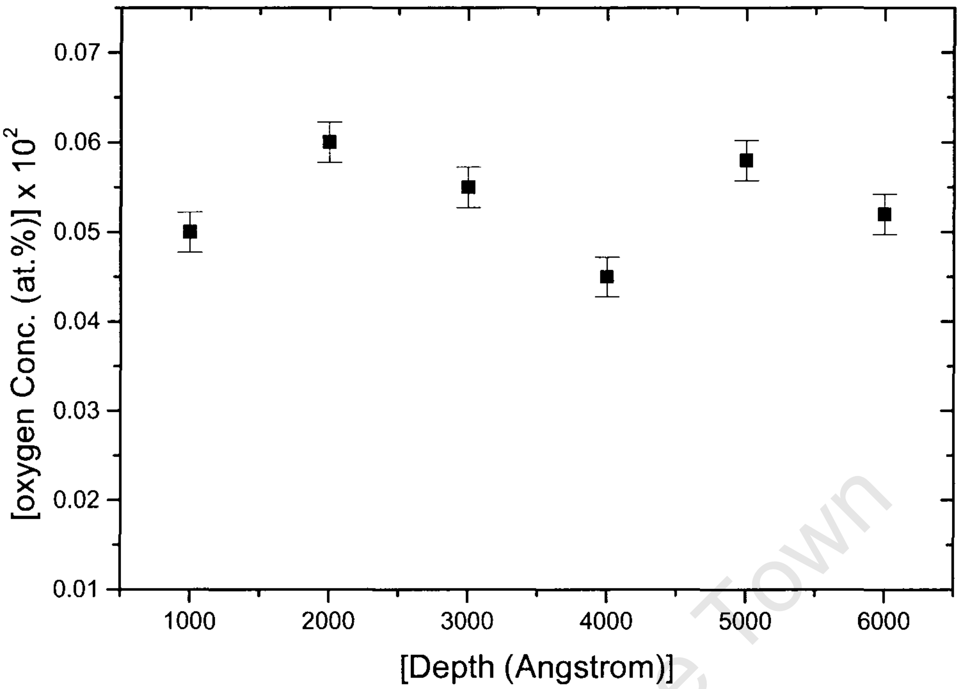

Figure 5.14(b): Shows the oxygen concentration against the depth in sample Mw136

Figure 5.15 (a) – (d) show similar spectra for sample Mw151. For this sample, which was deposited at high substrate temperature of 500°C, and pressure of 40 μbar, the spectra acquired revealed 2 at. % of oxygen at the resonance energy of 3.05 MeV (figure 5.15(a)). Subsequent increase of the probe energy revealed no such peak as it goes deeper into the sample. The incident beam energy was again raised to 3.45 MeV and subsequently to 3.75 MeV to detect other light element such as nitrogen and carbon ($^{12}C(\alpha, \alpha)C^{12}$:@ 3.55 MeV) [64] that might be present in the sample, but the absence of any such peak corresponding to resonance energies of these elements indicate its absence as shown in spectra of figure 5.16.

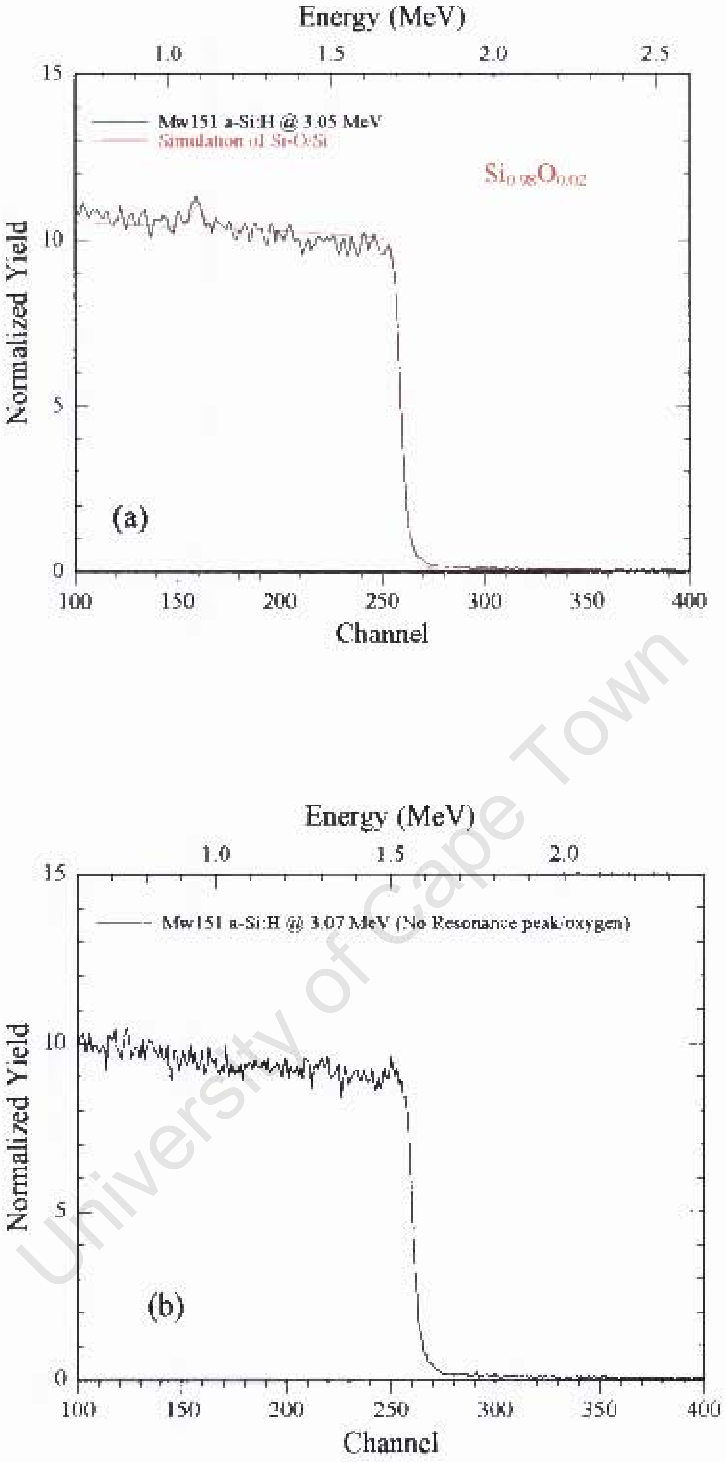

Figure 5.15(a): showing acquired spectra and simulation for sample Mw151, a less pronounced peak is noticed at 3.05 MeV, indicating presence of oxygen. But (b), (c), and (d) shows absence of resonance peak at different energies which signify the absence of oxygen on the sample as the beam penetrates deeper.

based devices [65, 66, 28]. More importantly, the strong influence of substrate temperature on the material growth reduces the hydrogen content over a high range of temperature change. Thus, the more reasons why the substrate temperature needs to be maintain as earlier discussed in section 2.2.1, because the substrate is being heated by radiation from three different sources which is described in detail by thermodynamic model elsewhere [28].

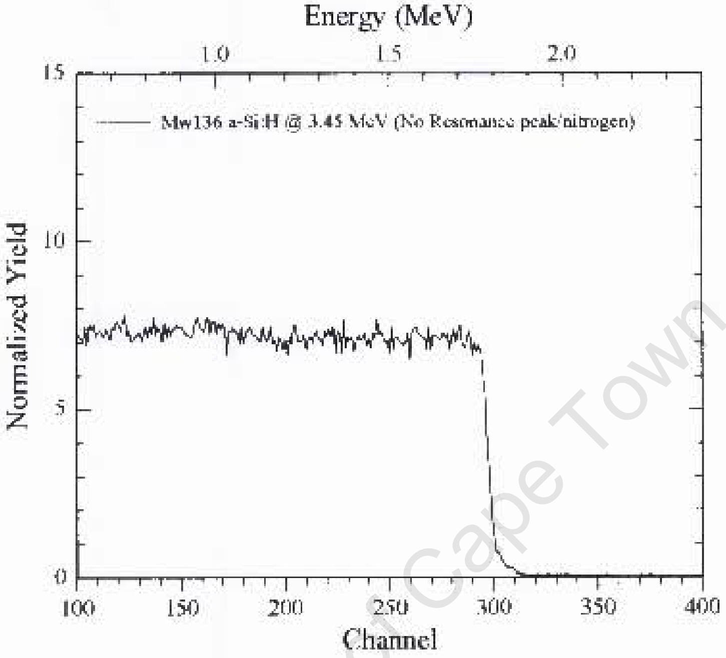

Figure 5.16: The spectra acquired when bombarded with incident energy beam of 3.45 MeV for detection of nitrogen and carbon, which was found to be absent.

RBS/resonance scattering was performed on Mw151 sample six months later along with another sample Mw150 which was deposited at 400°C under vacuum pressure of 40 μbar.

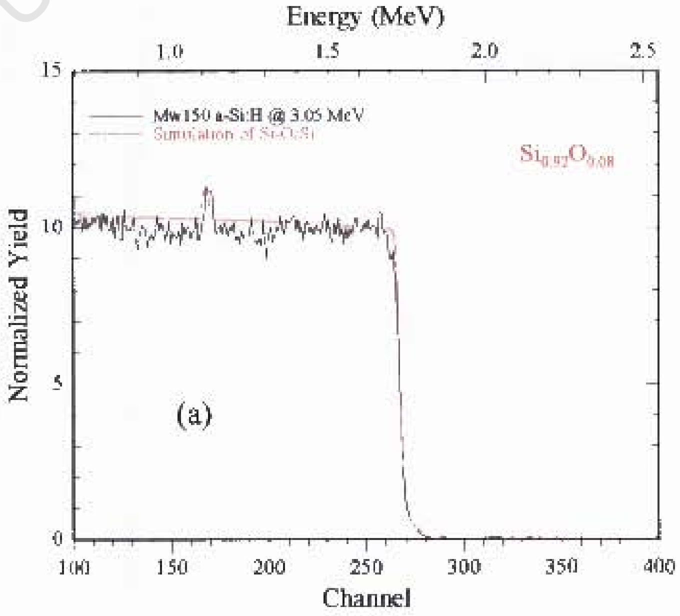

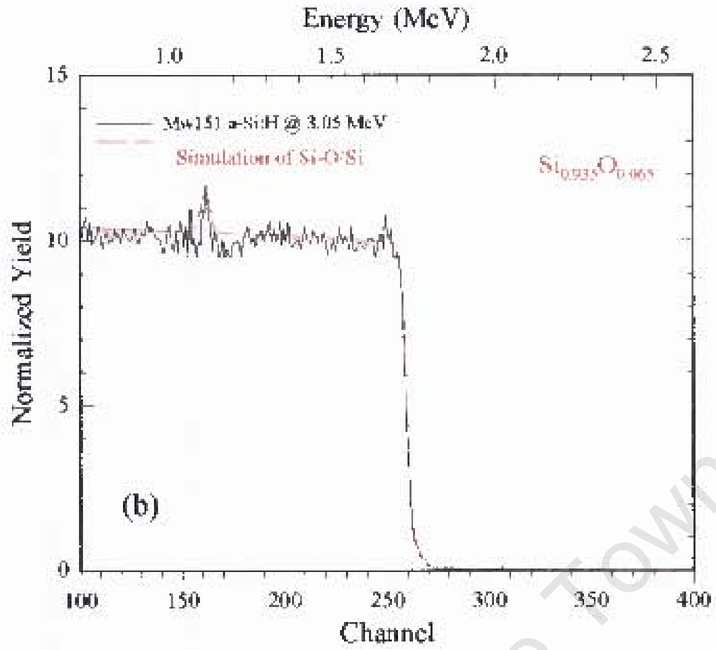

Figure 5.17 (a) and (b) show the spectra for Mw150 and Mw151 respectively at 3.05MeV after six month of deposition

The oxygen impurity yield at the resonance energy of 3.05 MeV varied between 7 at. % and 8 at. % for Mw151 and Mw150 respectively when simulated. The spectra, shown in figure 5.17 and 5.18, show similar patterns to the previous spectra analysed when bombarded with different beam energies, with no oxygen deeper in the sample in both cases.

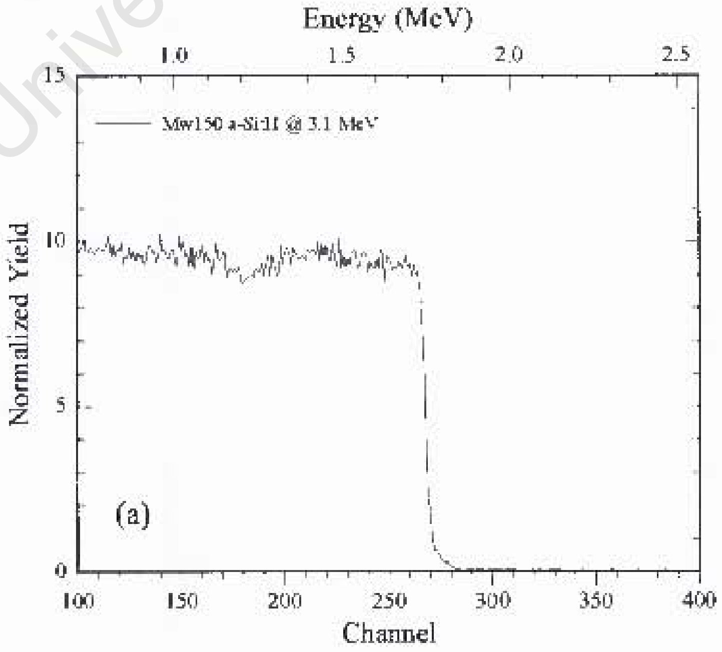

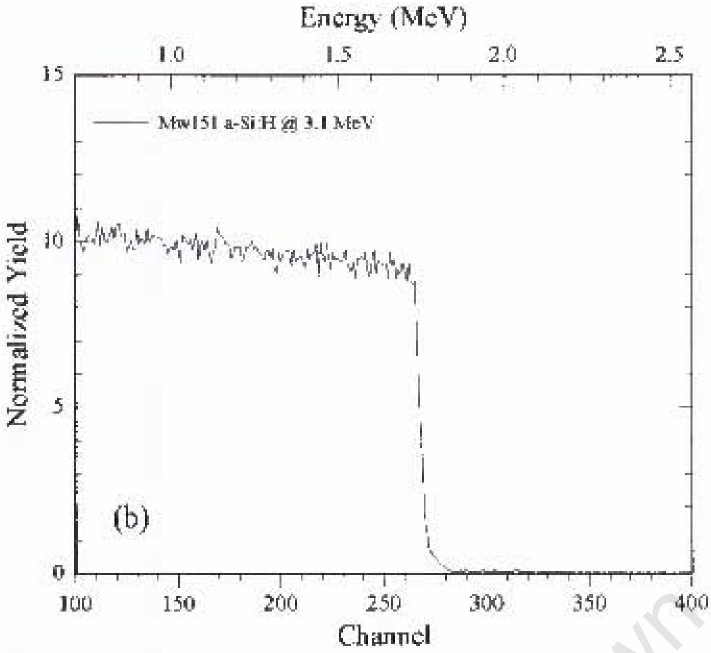

Figure 5.18(a) and (b): the same sample spectra at 3.10 MeV. The absences of resonance peak at this energy signify absence of light element distance deep into the sample.

5.1.1 RBS/Resonance scattering measurement on nanosilicon powder.

The method of analysis and measurement remain the same but what is unique about this measurement is the technique used in the preparation of the samples which was discussed in chapter 4. The nanopowders, which are made into palettes fitted well into the sample holder and were impinged with different beam energies.

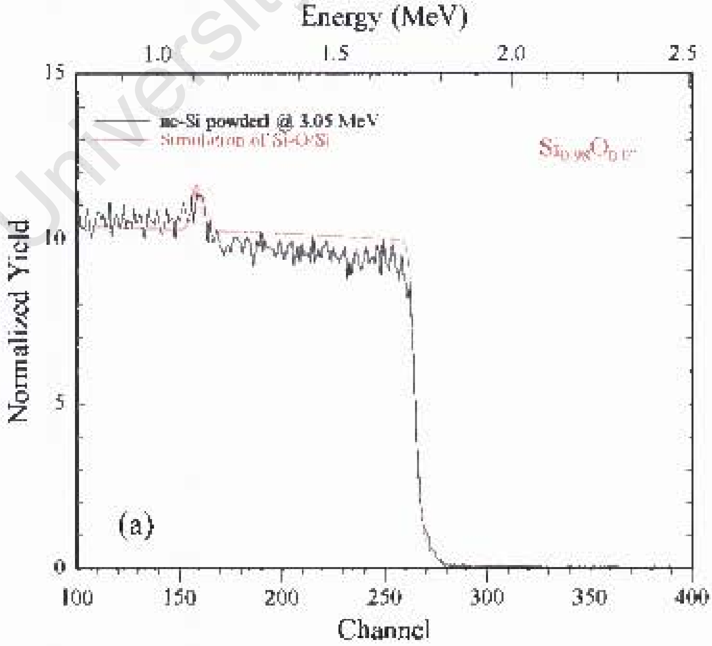

Figure 5.19(a): depicts simulation of spectra for nanosilicon powder immediately after preparation revealing less pronounced resonance peak near surface region of the sample.

The spectra acquired were simulated, and the results obtained are shown in figure 5.19 (a), (b), (c) and (d). The measurement was done immediately after the samples were prepared and a week later to see the effect of contamination or other atmospheric influences. The oxygen concentration was initially 2 at. % and rose to 6 at % thereafter. This appears to result from the oxidation process of silicon by air (moisture) when exposed.

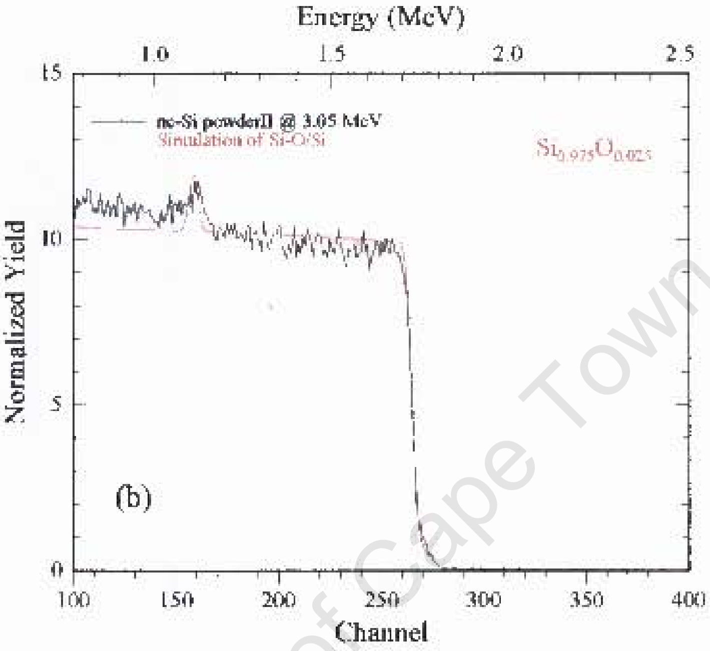

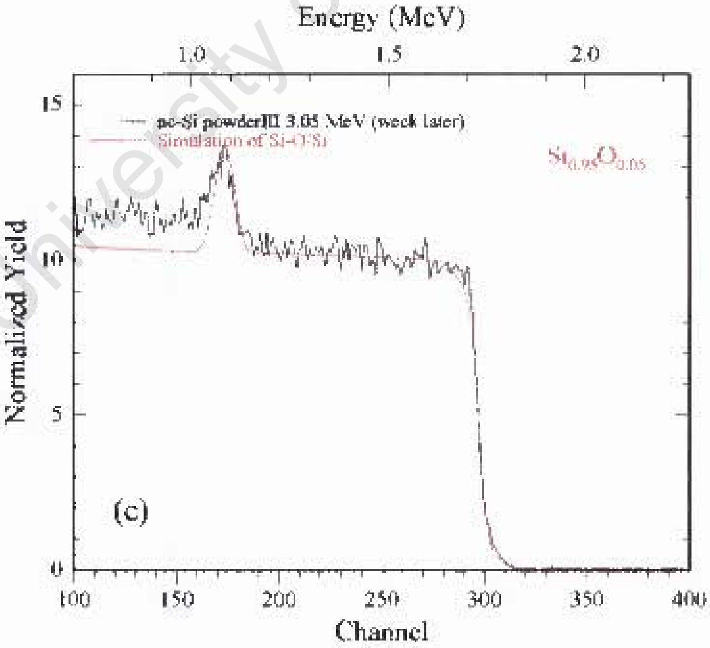

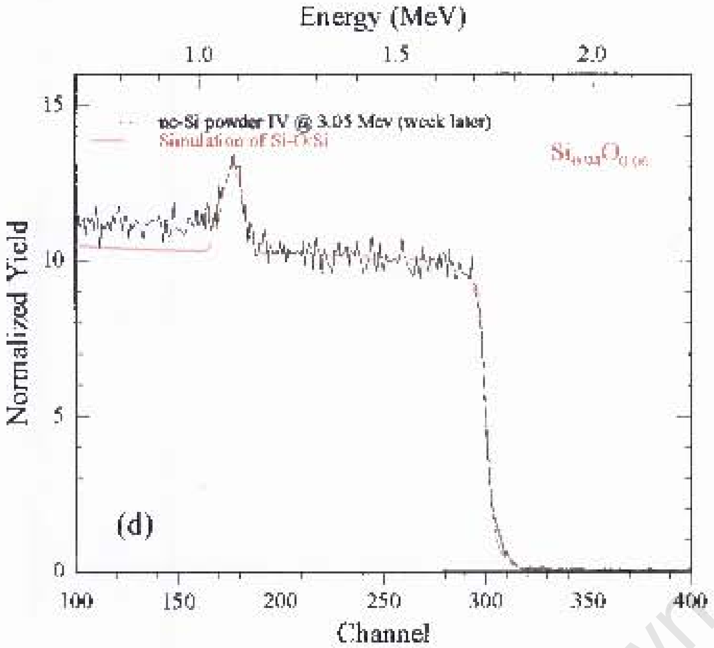

Figure 5.19: (c) & (d) depicts simulation of spectra for nanosilicon powder a week after preparation, a pronounced resonance peak is noticed at the near surface region of the sample.

5.2 Elastic Recoil Detection Analysis

The hydrogen content was determined using ERDA, for a-Si:H layers deposited under different conditions in two phases: as-deposited and after illumination for extended period as described earlier. The spectra acquired and simulated using the RUMP program are shown below:

5.2.1 Spectra for Hydrogen content as-deposition

Kapton foil was used as reference as discussed in section 4.2.3.2 and seen in figure 3.14. In figure 5.21 to 5.23, the simulations fitted with slight broadening at the leading edge of the experimental spectra, which is a feature that is common to most of the spectra. This feature could be attributed to the charges (Q) collected for certain irradiation time, which results in desorption of hydrogen from the surface of the samples. This effect is more pronounced in the spectra acquired after four hours of illumination. The height of the spectra acquired for ERDA analysis, unlike RBS spectra, gradually decreases toward the lower end of the channel. This is as a result of the dependence of the height on both the scattering cross-section and the stopping cross section [50, 67], so that the effective cross sections of the recoil atom increases at first and then decrease as a function of depth.

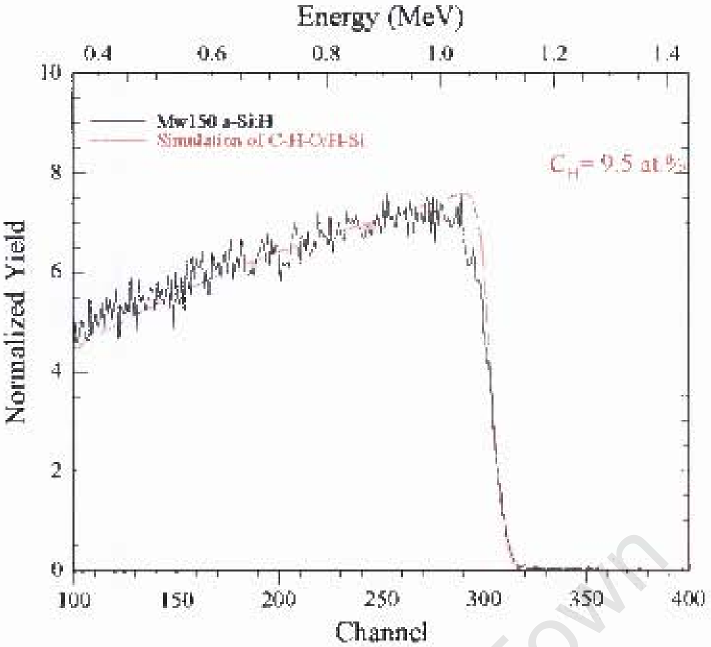

Figure 5.21: ERD spectrum and simulation obtained for a-Si:H sample Mw 150 having C_H of 9.5 at %

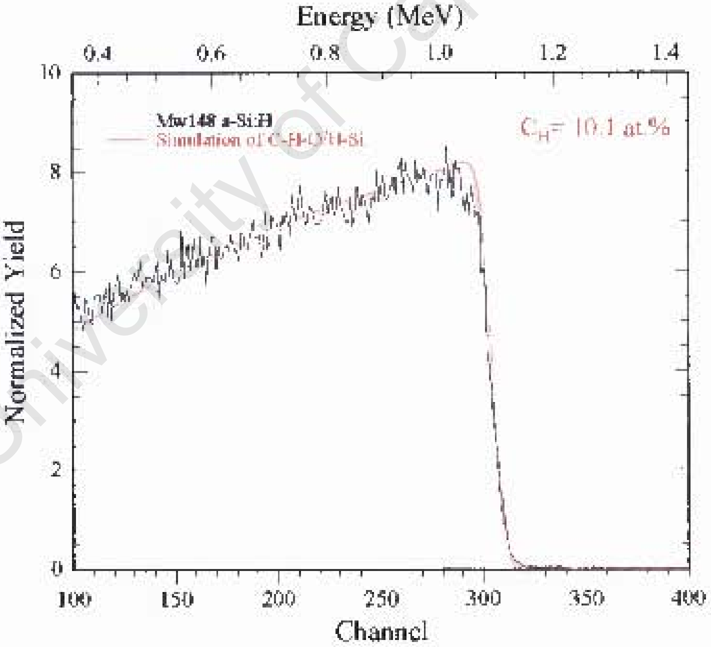

Figure 5.22: ERD spectrum and simulation obtained for a-Si:H sample Mw 148 having C_H of 10.1 at %

In figure 5.24, the widened differences in the experimental spectrum and the simulation down to the lower energy (channel number) indicate, the constant recoiling of hydrogen atoms with decreasing energy resulting from irregular hydrogen concentration in the sample.

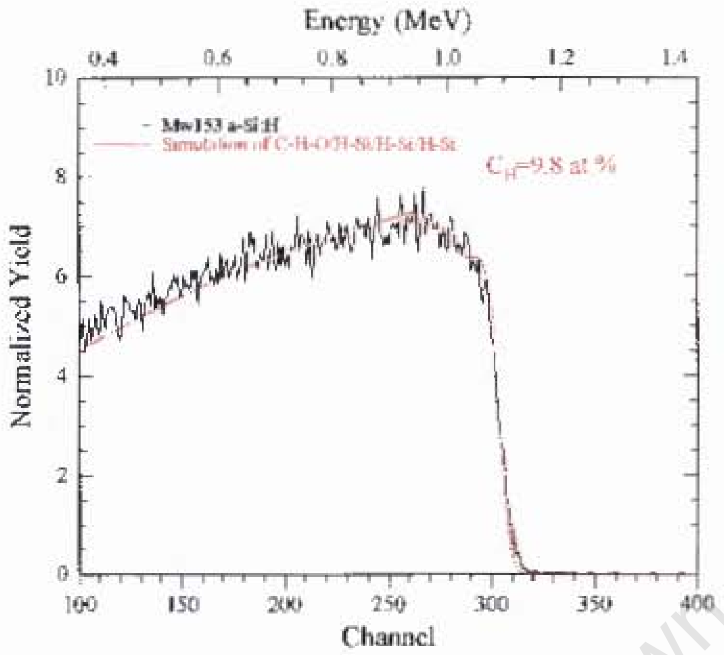

Figure 5.23: ERD spectrum and simulation obtained for a-Si:H sample Mw 153 having C_H of 9.8 at %

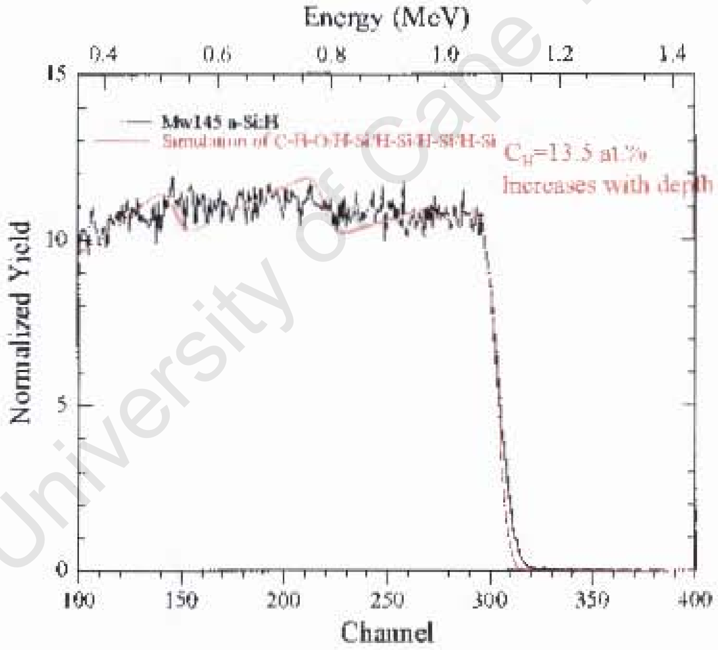

Figure 5.24: ERD spectrum and simulation obtained for a-Si:H sample Mw 145 showing irregular distribution of hydrogen in the a-Si network, 13.5 at.% at the surface and its increases with depth.

For figure 5.25, the difference in the experimental spectrum and simulation at the channel number between 100 and 150 is due to double scattering, which might have resulted from small fluctuation of hydrogen concentration slightly below the surface of the sample or the variation in the hydrogen recoils well below the surface and

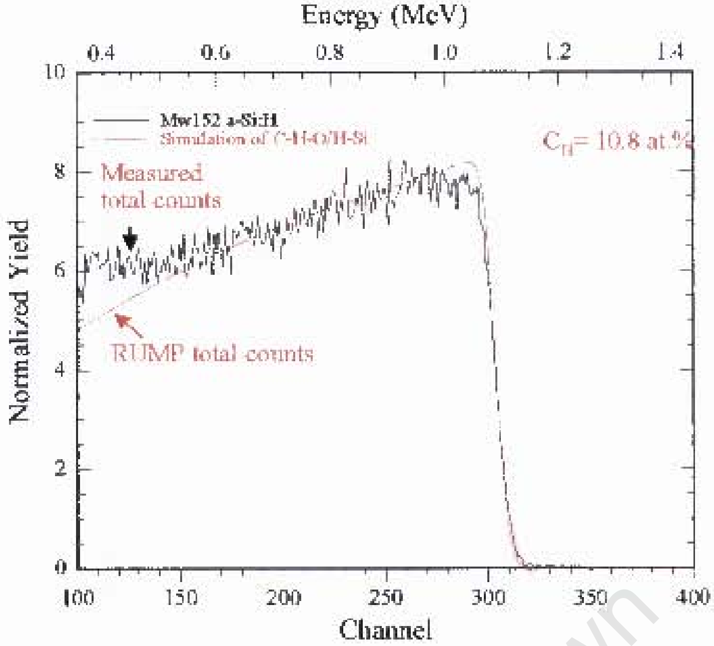

Figure 5.25: ERD spectrum and simulation obtained for a-Si:H sample Mw 152 having C_H of 10.8 at %

that recoils closer to the surface. Another sample, Mw136, in figure 5.27 revealed a high surface peak, which is a feature that is not found in any other sample analysed. The results from the simulations in figure 5.21 – 5.29(a), reveal that the hydrogen concentration in the amorphous network ranges from 9.5 to 11.3 at. %. Fig. 5.29 (b) also shows the plot of the substrate temperature against hydrogen content.

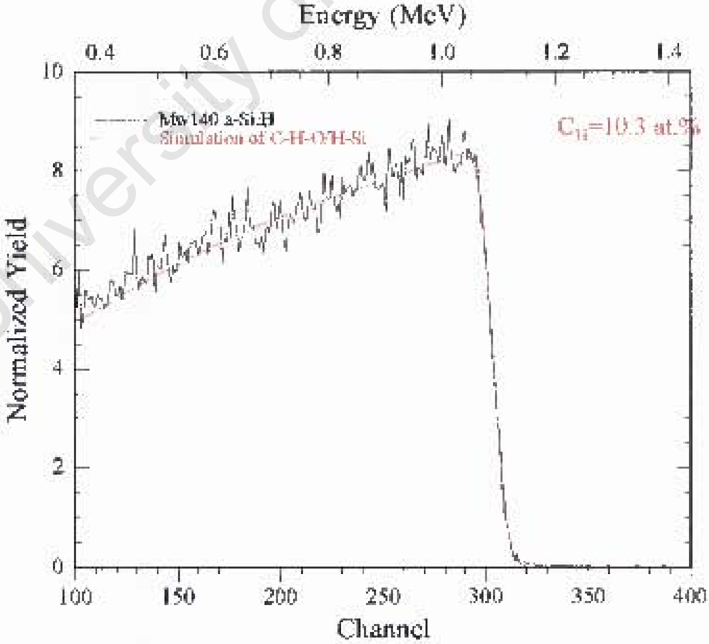

Figure 5.26:ERD spectrum and simulation obtained for a-Si:H sample Mw 140 having C_H of 10.3 at %

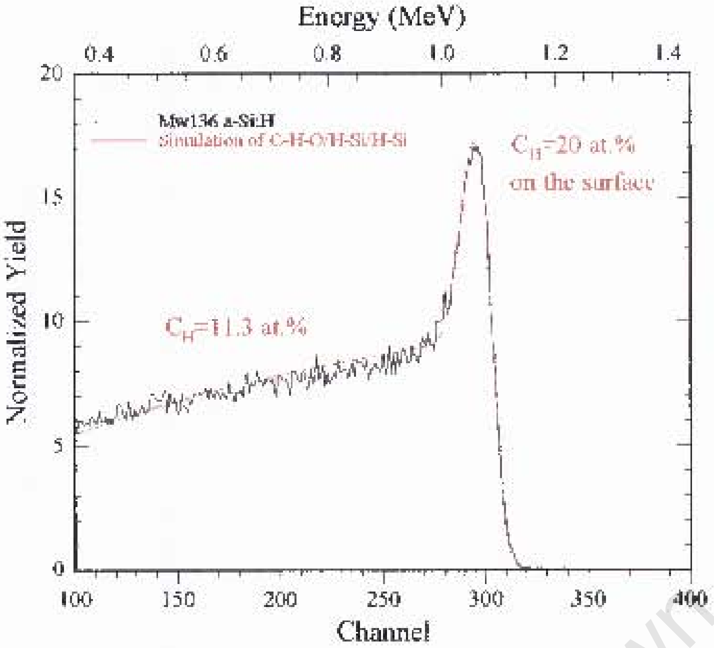

Figure 5.27 ERD spectrum and simulation obtained for a-Si:H sample Mw 136 having C_H of 11.3%and 20% on the surface region of the sample.

The graph revealed fluctuation of the hydrogen content within those ranges of substrate temperature, however the deposition process is consider under two pressure conditions: high (80μbar) and low (40μbar). For high pressure deposition the samples Mw 136, Mw139, Mw140 and Mw141 have hydrogen contents of 11.3, 11.3, 10.3 and 9.9 at. %

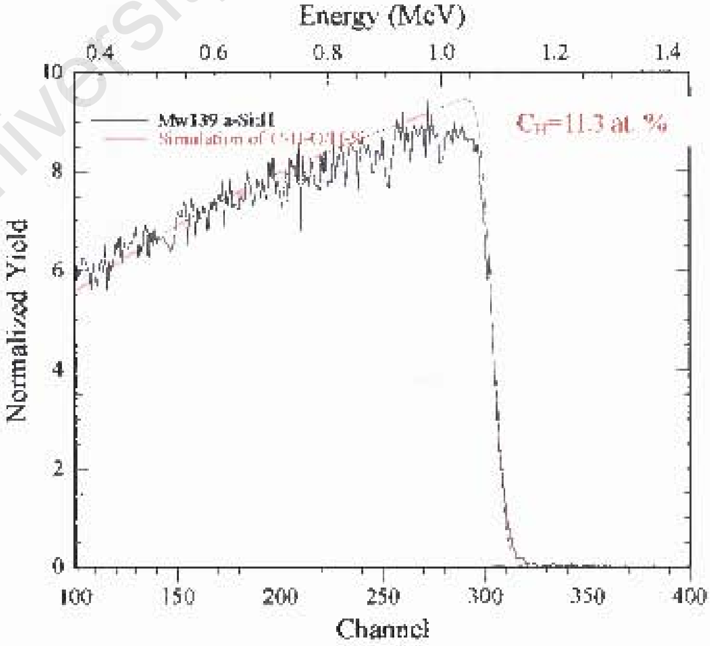

Figure 5.28: ERD spectrum and simulation obtained for a-Si:H sample Mw 139 having C_H of 11.3 %

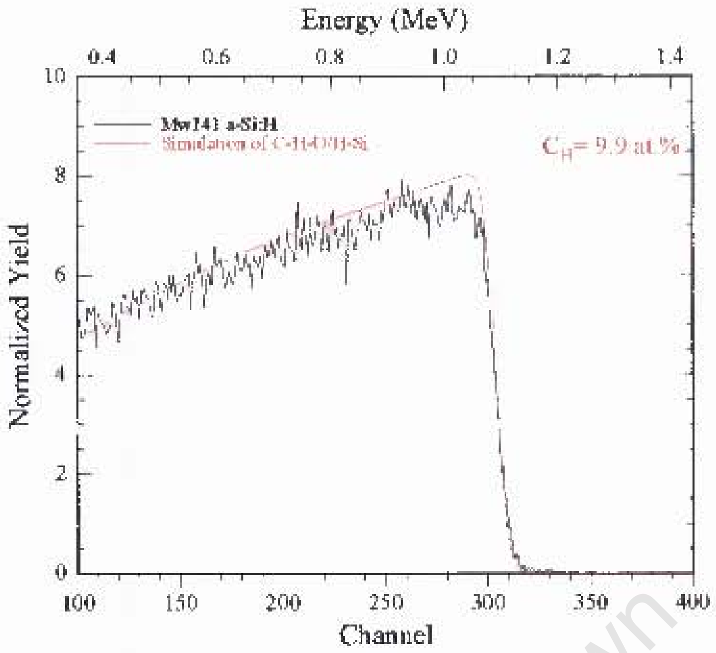

Figure 5.29: ERD spectrum and simulation obtained for a-Si:H sample Mw 141 having C_H of 9.9 at %

Respectively, while those deposited at lower pressure Mw145, Mw148, Mw150, Mw151, Mw152 and Mw153 contained 13.5, 10.1, 9.8, 9.5, 10.8 and 9.8 at. % respectively. It is expected that with increase in deposition (substrate) temperature the hydrogen content reduces [65, 66, 28]. However, the variation and fluctuation of the hydrogen content may be attributed to predominantly influx of higher hydrides in the gas phase due to increase in the silane consumption under high pressure, which in turn results in more production of atomic hydrogen. Variation or alteration

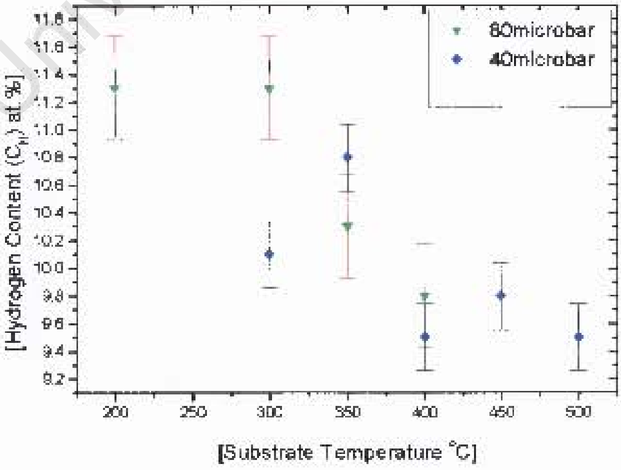

Fig. 5.29(b): Substrate temperature against the hydrogen concentration

of the pressure to the lower end, results in insufficient diffusion of atomic hydrogen in the gas phase into deposited amorphous material [26].

5.2.2 Hydrogen Content after illumination

The samples were illuminated after the initial measurement for 4hrs and 8hrs with a halogen lamp of 100 W/m^2 intensity. The blunt edges of the spectra (figure 5.30 – 5.33) acquired under 4hrs illumination appear to be as a result of more exposure than necessary of the beam energy to the samples in the chamber during measurements, which is a feature that is more prominent to all samples measured at this time. An average of 2 at.% were depleted over a depth of 200 nm from the surface of the samples during the irradiated time.

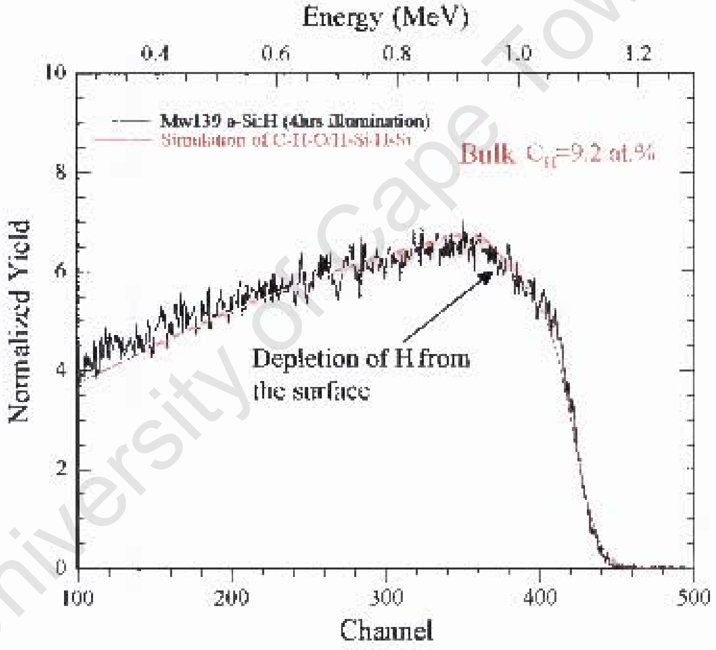

Figure 5.30: ERD spectrum and simulation obtained for illuminated a-Si:H sample Mw 139 having C_H of 9.2 at % in the bulk and a C_H of 7.2 at.% in surface region.

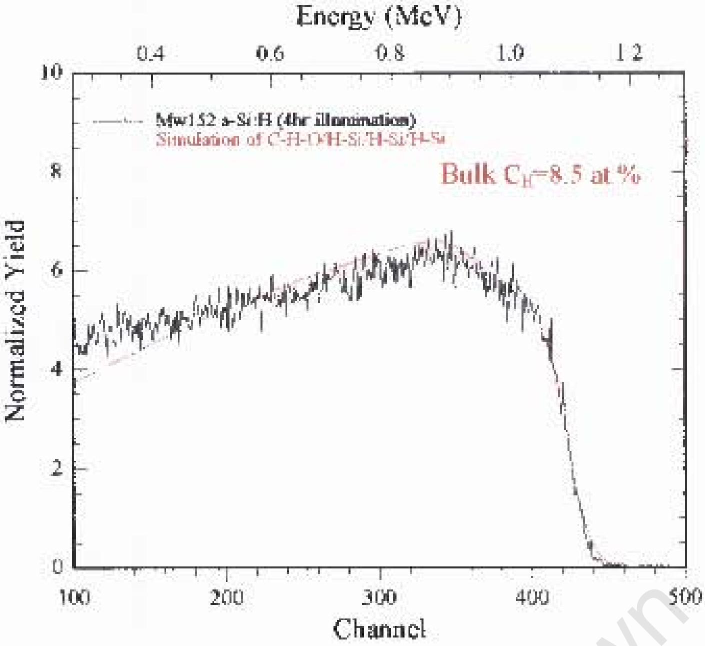

Figure 5.31: ERD spectrum and simulation obtained for illuminated a-Si:H sample Mw 152 having C_H of 8.5 at % in the bulk and a C_H of 6.7 at.% in the surface region

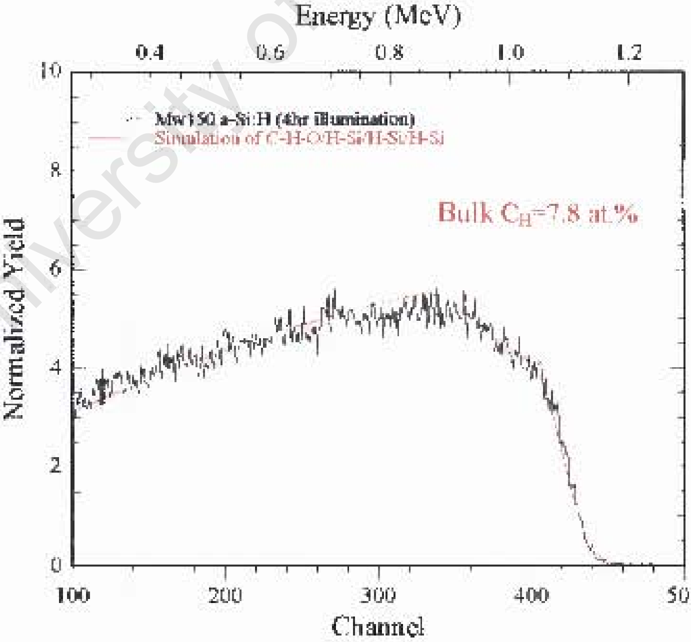

Figure 5.32: ERD spectrum and simulation obtained for illuminated a-Si:H sample Mw 150 having C_H of 7.8 at % and a C_H of 5.6 at. % in the surface region

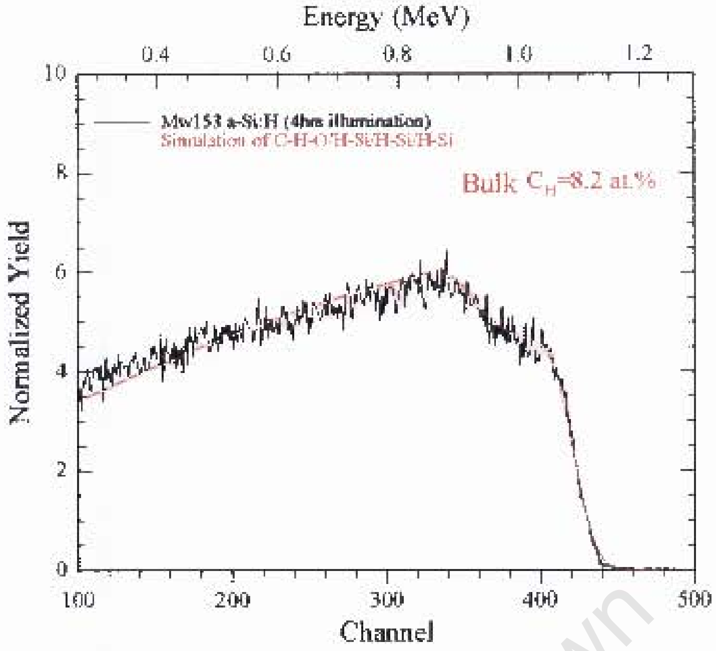

Figure 5.33: Simulation of ERD spectrum obtained for illuminated a-Si:H sample Mw 153 having C_H of 8.2 at. % and a C_H of 6.4 at. % in the surface region

For the eight hours illumination, the spectrum of sample Mw151 (figure 5.38) showed a special feature which is quite different from the others, a U-shape near the surface. When simulating, the spectrum was simulated over three layers, with the middle layer having lower hydrogen content.

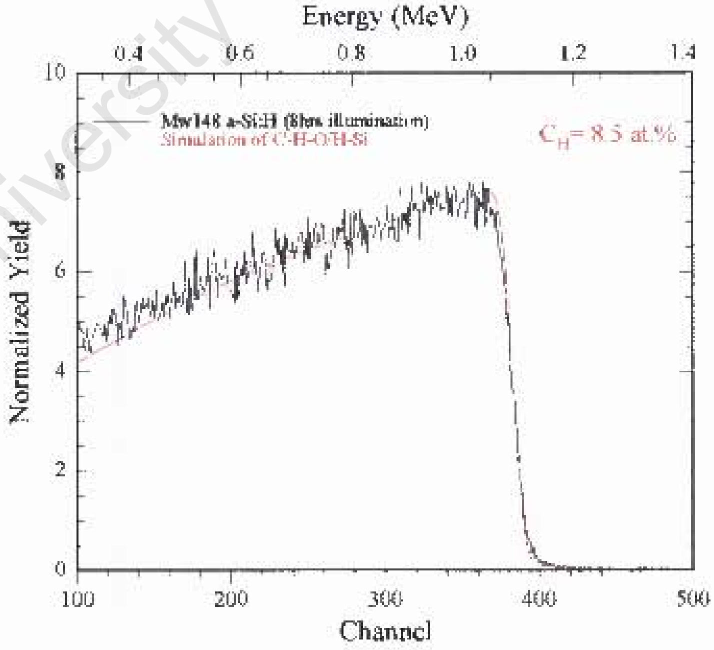

Figure 5.34: ERD spectrum and simulation obtained for eight hours illuminated a-Si:H sample Mw 148 having C_H of 8.5 at %

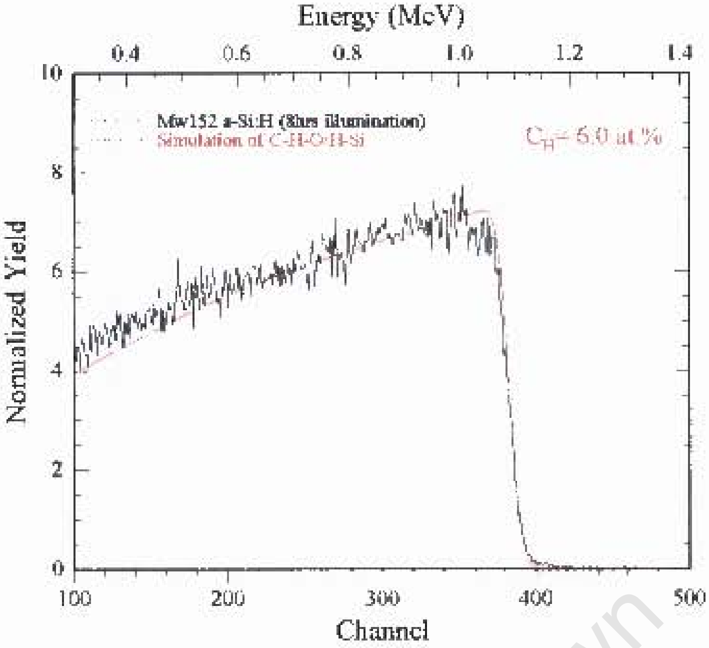

Figure 5.35: ERD spectrum and simulation obtained for eight hours illuminated a-Si:H sample Mw 152 having C_H of 6.0 at %

This appears to be due to a sort of movement or migration of hydrogen within the network after illumination. Also, a small peak of 60 nm thick was observed on sample Mw150, which corresponds to surface hydrogen.

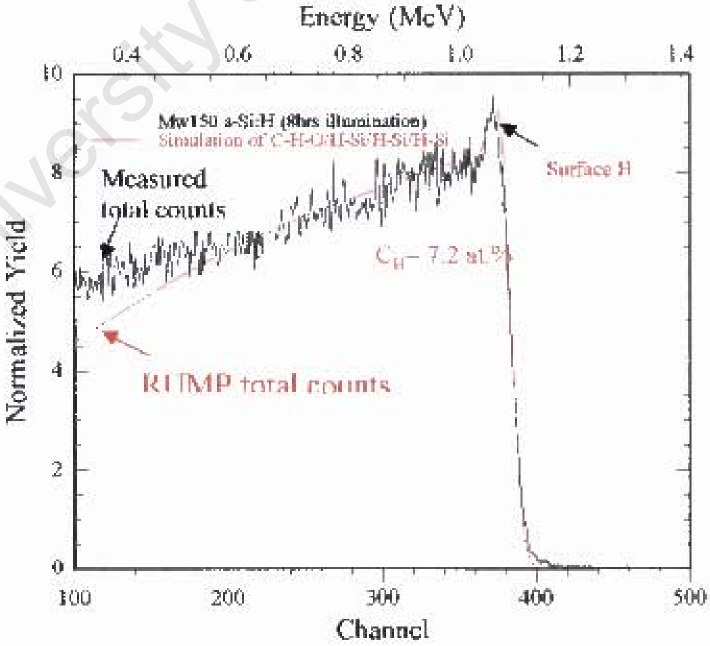

Figure 5.36: ERD spectrum and simulation obtained for illuminated a-Si:H sample Mw 150 having C_H of 7.2 at %

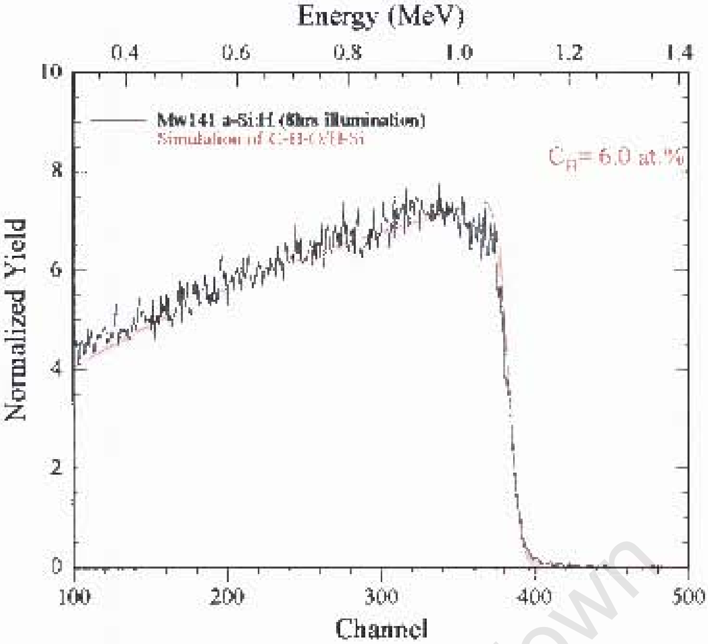

Figure 5.37: ERD spectrum and simulation obtained for eight hours illuminated a-Si:H sample Mw 141 having C_H of 6.0 at %

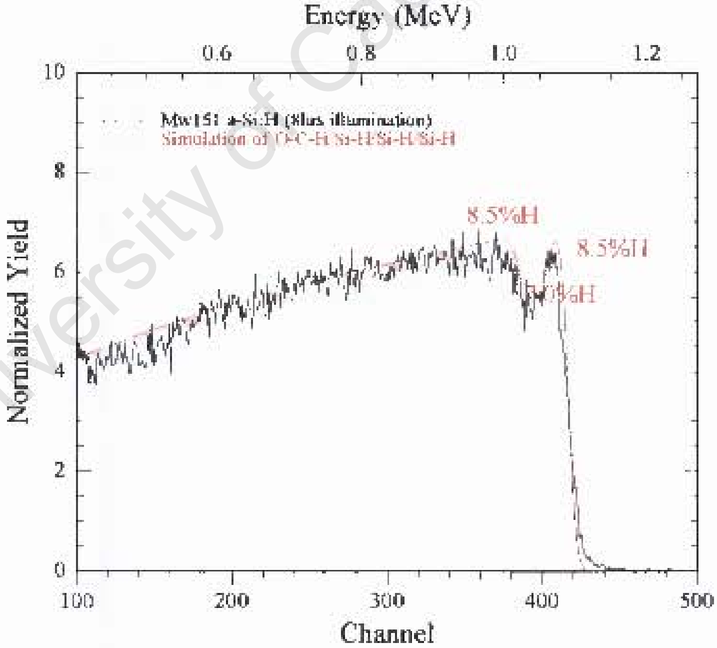

Figure 5.38: ERD spectrum and simulation obtained for eight hours illuminated a-Si:H sample Mw 151 having C_H of 8.5 at %

5.2.2 Hydrogen content: Nanosilicon powder

The nanopowder silicon samples were also measured for hydrogen content using ERDA. The data and simulated spectra are shown in figures 5.39 and 5.40 for the same powder immediately after preparation and after one week under ambient conditions respectively. In the figures the scale for the recoiled H yield is low compared to the a-Si:H measurements shown in the previous section. Despite allowing the samples to stay for a week as done with RBS/resonance scattering, the hydrogen contents only varied between 1.0 at.% and 1.2 at. % for all samples.

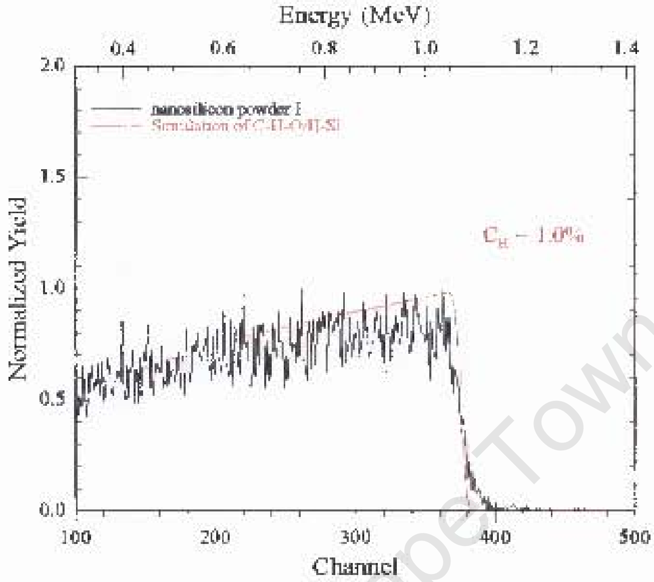

Figure 5.39: ERD spectrum and simulation obtained for nanosilicon powder sample having C_H of 1.0 at %

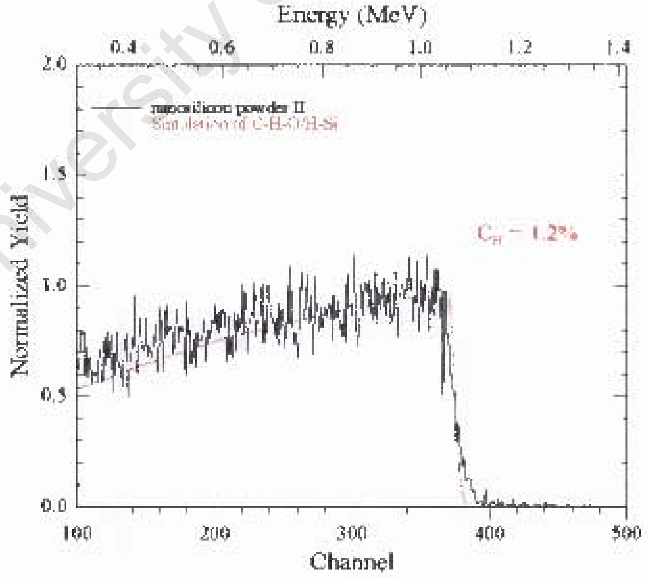

Figure 5.40: ERD spectrum and simulation obtained for nanosilicon powder sample having C_H of 1.2 at %

5.3 Scanning Electron Microscopy

For the hydrogenated amorphous silicon sample, micrographs were taken in the as-deposited condition and after various intervals up to twenty four hours illumination. The samples illuminated for four and eight hours showed no appreciable difference to the as-deposited state, and the results are not shown. Figure 5.41 depicts the as-deposited micrographs of samples Mw136 and Mw151, which have different deposition parameters. Mw151 is deposited at a higher temperature and lower pressure while Mw136 is deposited at a lower temperature and high pressure. There is an obvious different in morphology of the two samples, with the layer deposited at the lower temperature (Mw136) being less compact and having a cauliflower like structure. The micrographs of sample Mw 145, Mw150, Mw152 and Mw153, comparing as-deposited against the illuminated samples, figure 5.41 to 5.43 shows that only for Mw145 (figure 5.42) there is a clear change on illumination, with the larger becoming a smoother, which could be due to a densification of the a-Si:H. There is also an appearance of a striated structure in Mw145 and Mw150 on illumination, which does not occur in other two samples.

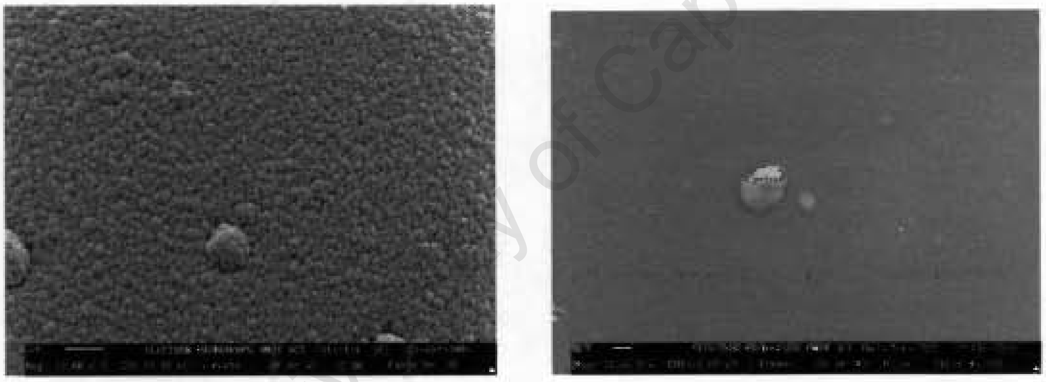

Figure 5.41: Micrograph of sample Mw136 and Mw151 deposited at 300°C and 500°C respectively

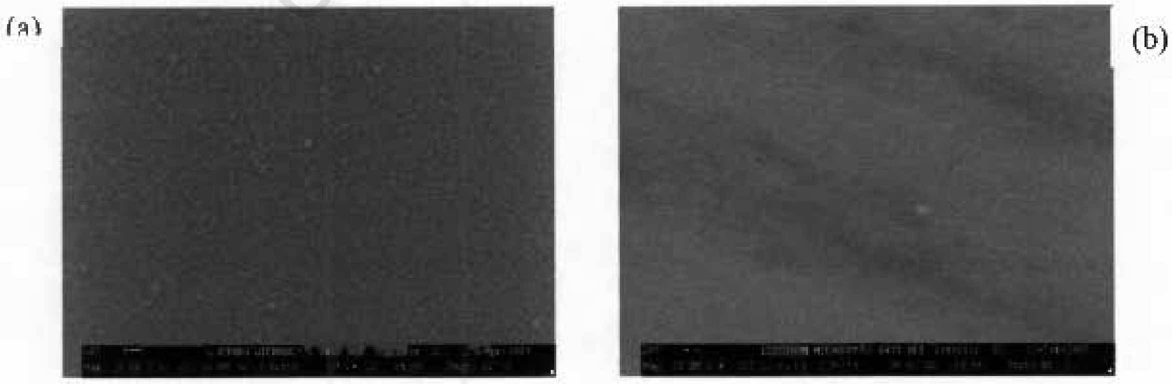

Figure 5.42: Micrograph of sample Mw145 as- deposited (a) and after illumination (b)

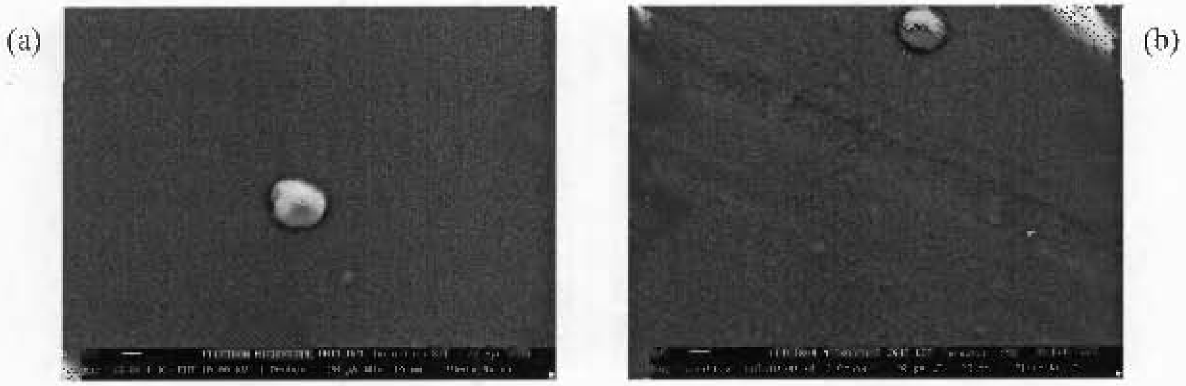

Figure 5.43: Micrograph of sample Mw150 as- deposited (a) and after illumination (b)

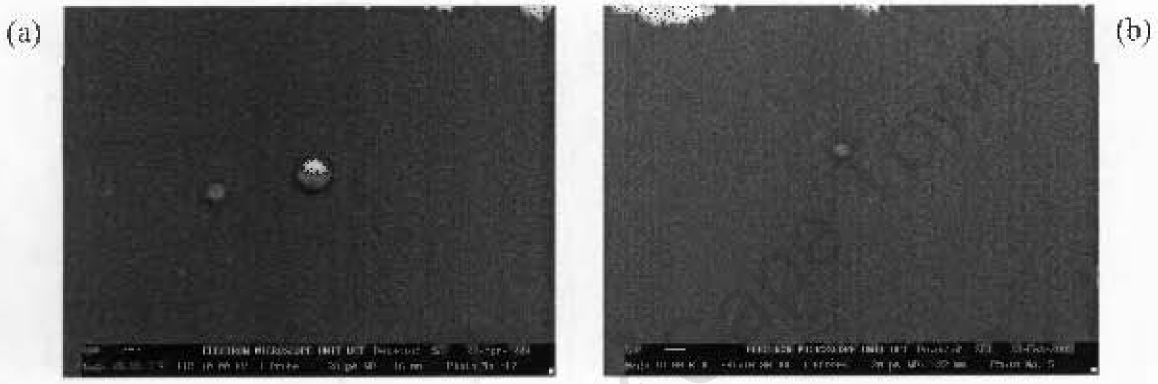

Figure 5.44: Micrograph of sample Mw152 as- deposited (a) and after illumination (b)

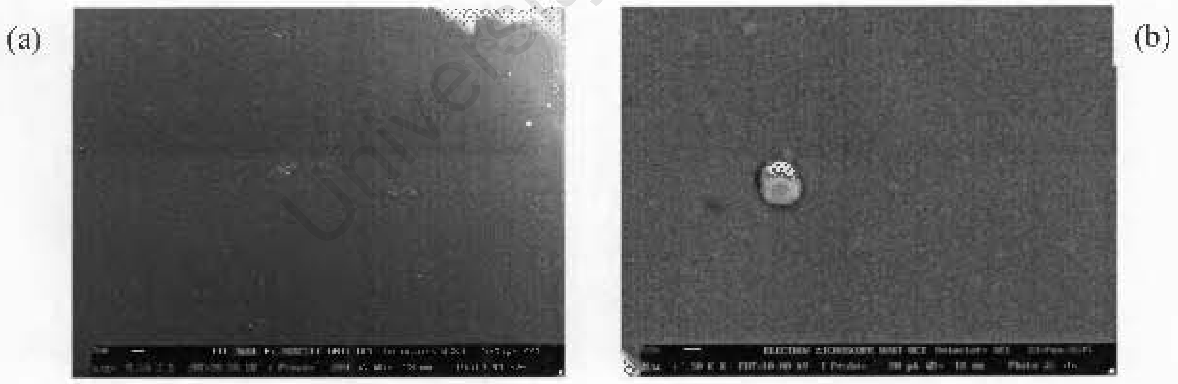

Figure 5.45: Micrograph of sample Mw153 as- deposited (a) and after illumination (b)

6 DISCUSSION

Elastic recoil detection analysis is used in determining the hydrogen content in both hydrogenated amorphous and nanocrystalline silicon. Hydrogen incorporation into the amorphous silicon network is to passivate the dangling bonds, and also, introduction of hydrogen will enhance the structural reordering and relaxation in the network [5]. However, the Staebler-Wronski effect is often related to the hydrogen content in hydrogenated amorphous silicon [68]. To this end, this measurement gives the total hydrogen content, in atomic percentage by using the RUMP simulation program over the acquired spectra. The total hydrogen is the sum of the bonded hydrogen and the molecular hydrogen [69, 70]. The total hydrogen concentrations for the a-Si:H samples are summarised in table 6.1.

Table 6.1: Hydrogen concentration as-deposited and after illuminations

Samples	***Deposition temperature***	***H atomic% As-deposited***	***H atomic % after 4hrs illumination***	***H atomic % after 8hrs illumination***
Mw 136	300	11.3	-	-
Mw 139	200	11.3	9.2	-
Mw140	350	10.3	-	-
Mw 141	400	9.9	-	6.0
Mw 145	250	Irregular distribution of Hydrogen	Irregular	Irregular distribution of Hydrogen
Mw 148	300	10.1	-	8.2
Mw 150	400	9.5	7.8	7.2
Mw 151	500	9.5	-	8.5
Mw 152	350	10.8	8.5	6.0
Mw 153	450	9.8	8.2	-

Illumination of the samples was done with halogen light intensity of 100 W/m^2 for four and eight hours, to observe and determine the role of hydrogen in degradation (Staebler and Wronski effect) of these samples. Figure 6.10 shows the downward trend of hydrogen contents as-deposited, and upon illumination for four and eight hours respectively.

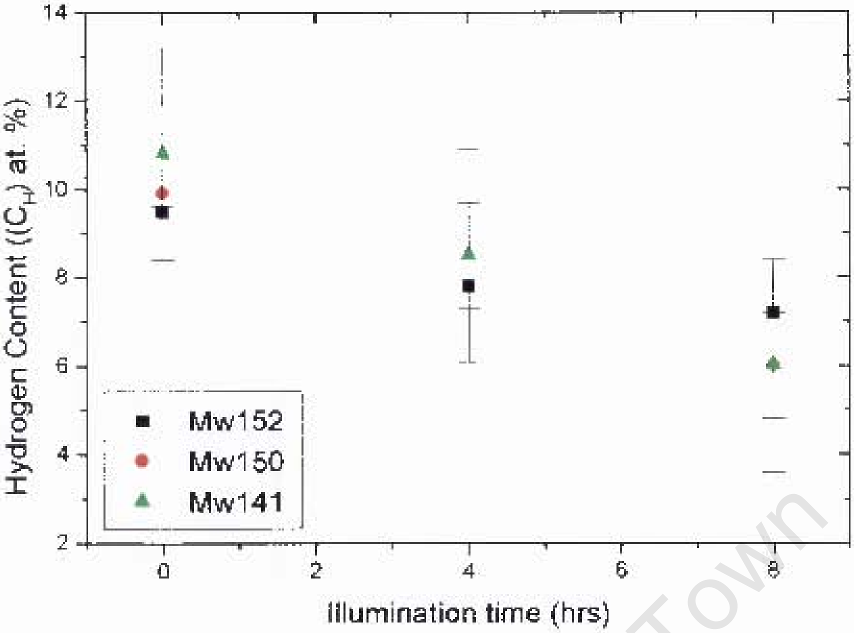

Fig. 6.10 the trend of hydrogen content with illumination time

From the foregoing, increasing the illumination time decreases the hydrogen content, hence this induces defect into the amorphous material, since hydrogen incorporation into amorphous silicon passivates the dangling bonds, reduces the stress state and also reduces the density of states in the band gap. The defects are induced by the energy supplied by illuminating (light soaking) the samples, which breaks the weak Si-Si bond thus producing a dangling bond. Formation of dangling bonds has been one of the factors contributing to degradation in a-Si:H solar cells, and it has been found that it takes about 10^7 photons to produce a dangling bond [4]. Since dangling bonds act as a recombination or trapping centres, increase in the illumination intensity will favour an increase in the volume of dangling bonds resulting in more available centres for the electron-hole pair recombination process [6]. This is experimentally seen by the change in hydrogen content as the sample is illuminated, though the decrease is not of regular magnitude. Sample Mw151 revealed a different feature to the other samples after illumination for eight hours: a U-shape near the surface region of the sample, with less hydrogen in between and with thickness of 80nm. Also, is a small peak of 60nm on sample Mw150, these could be attributed to the movement or migration of H in the amorphous network

[71]. Also, formation of more hydrides or di-hydride complexes was observed by FTIR results, when comparing with this technique that was performed by another member of the group. The bonding configuration and bonded hydrogen content of amorphous samples were determined using the Perkin-Elmer Fourier transform IR spectrometer, of which the bonded hydrogen contents were calculated by the numerical integrations of the Si-H wagging mode (640cm^{-1}) as seen in table 6.2. The bonded hydrogen concentration in a-Si:H samples were all systematically lower than the total concentrations determined by the elastic recoil detection technique, but followed the same trends. In addition, after illumination an additional mode at 3000 cm^{-1} corresponding to the C-H bond [23] was observed. The structural changes implied by the appearance of FTIR modes corresponding to di-hydride complexes are also evident when comparing the topological structures of the samples [as-grown and illuminated (figure 5.42-5.45)]. Electron microscopy shows the appearance of a smoother surface with some striation lines.

Table 6.2: Comparison of the hydrogen contents

Samples	*Substrate Temp (oC)*	*Thickness of the layer (nm)*	*Hydrogen atomic % FTIR/UV*	*Hydrogen atomic % ERDA*
Mw153	450	1320	5.2	9.8
Mw152	350	1550	7.7	10.8
Mw 150	400	2800	-	9.5
Mw145	250	2500	11.6	*Irregular distribution of Hydrogen*
Mw 141	400	3900	-	9.9

Although, as seen in table 6.1, the total hydrogen content averages around 10%, irrespective of the growth temperature, the bonded hydrogen concentration decreases systematically with increasing temperature. This suggests that although the structure grown at higher temperatures is becoming better ordered, with less H terminated bonds, the fraction of total H content increases. The site of this molecular hydrogen is still not clear, but it may be trapped in nanovoids or at grain-boundary-like regions.

The observation that the total hydrogen content does not depend on the substrate temperature strongly suggests that this is determined by the flux of hydrogen during the deposition process. This in turn is determined only by the gas parameters.

One of the samples Mw145 was seen to have a different spectrum, which when simulated gives a different result. It appears that the hydrogen content is more in this sample, which is about 13.5 at. % at the near-surface region and increases gradually with depth to 18.0 at. %. Unlike the other samples, which has an average of 10 at. % concentration in the bulk. The FTIR measurement of this sample showed that the C-H vibrational mode was more pronounced, which suggests possible contamination of carbon in the sample. Furthermore, the measurement showed that the peak at C-H vibrational mode may have resulted from the excess hydrogen atoms bonded to carbon impurities. However, the presence of carbon in this sample still remains to be investigated with resonance scattering for this sample.

Another anomaly noticed was in sample Mw136, which showed a sudden sharp peak (figure 5.27). Investigation as to what might have caused it was carried out with another sample. This was allowed to undergo RBS/Resonance scattering measurement and elastic recoil detection analysis thereafter, to see if the peak was due to damage as a result of high incident beam, but it was negative. Furthermore, the Mylar foil was viewed under the optical microscope to see if there is any perforation due to over-usage which might have weakened the foil, and allowed the helium ions to reach the detector. The micrograph revealed few perforations to be present, though, its effect cannot be ruled out. The sharp peak appears to be as result of some organic contaminants present on the sample surface [72], because the hydrogen content on the surface is 20 at.%, which might have been introduced during mounting of the samples for analysis. The details of the simulation of the acquired spectra are shown in chapter five.

Another observation was the presence of a shoulder at the surface as seen in figure 5.30 – 5.33, which were from all the samples illuminated for four hours. RUMP simulation suggested that this shoulder corresponds to a depletion of H from near surface region of approximately 2.0 at. %. Since all of these samples had been irradiated for longer than necessary [73, 74], due to the adjustment of the signal amplifier. It is thought that this depletion was due to irradiation damage.

The scanning electron micrographs showed no significant changes in the topological view after eight hours of illumination but some changes were noticed after illumination for 24hrs as seen in figure 5.42-5.45, which was earlier mentioned.

The investigation by RBS/resonance scattering revealed a significant amount of oxygen contaminant present both in hydrogenated amorphous silicon and nanosilicon powder. The simulation overlaid onto the measured spectra revealed the amount of the oxygen impurities in atomic percentage in samples of hydrogenated amorphous silicon and nanocrystalline silicon powders. The two amorphous samples, which were deposited under different deposition conditions (see table 4.1 for deposition parameters) showed different concentration of oxygen. Sample Mw 136 revealed an average of 5 at. % oxygen (see figure 5.12) in the sample, while sample Mw 151 revealed only 2 at %.

Further investigation to probe the depth of this element revealed that in sample Mw 136 (containing 5 at %) oxygen is uniform throughout the sample, while in Mw151 it is only in the near surface region. This is consistent with what has been investigated in previous studies by different analytical techniques [2, 24]. Figure 5.13 shows the depth of oxygen in the sample as the resonance peak gradually shifts to the lower energy channel (left hand side) of the spectrum as the incident beam energy is increased. This also showed the concentration of the impurity element to be uniform throughout the sample. The measurement six months later showed that sample Mw150 and Mw151 now had concentrations of 8 at. % and 7 at. % respectively, but only on the surface of the samples. The exposure of sample Mw151 to air for some months caused little increase in deep oxygen impurities, likewise for sample Mw150, indicating the high compact nature of the material and its stability against oxidation. This was also observed by scanning electron microscopy. The topological view showed a compact stucture for sample Mw151, as seen in figure 5.41., and a granular surface for Mw136, which made this sample vulnerable to oxidation during and post deposition [24].

An attempt was made to probe for carbon using the $^{12}C(\alpha, \alpha)C^{12}$ resonance at 3.55 MeV [65] and nitrogen using $^{14}N(\alpha, \alpha)N^{14}$ resonance at 3.45 MeV [52], by raising the beam energy in steps of 0.03 MeV to 3.75 MeV. No resonance peak were observed in the spectra indicating that if there was any C or N contamination it was below the detection limit of the system.

Investigation of the nanosilicon powder samples which were prepared, as explained in section 4.1.2 and analysed immediately and a week later, showed that 2 at % of oxygen is present in the sample immediately after preparation. After one week, this increases to 6 at. % as seen in figures 5.18 and 5.19 respectively. This increase can be attributed to surface oxidation of the particles, which, however, is much thinner than the native oxide on bulk silicon. For particles of this size, 6 at. % of oxygen corresponds to approximately one monolayer of oxide. The analysis of these powder samples with elastic recoil detection analysis (ERDA) revealed only a very little hydrogen, typically, 1.0 – 1.2 at. %., which remains unchanged after a week exposure to ambient conditions. The low hydrogen content is consistent with the particles being highly crystalline and compact compared to a-Si:H. At this stage, it is not clear whether the hydrogen is incorporated in the particles or is only present at the surface. However, as the concentration remain constant, the former is most likely.

7 CONCLUSION

In this work, characterization of hydrogenated amorphous silicon and nanocrystalline silicon powder has been done using the combined techniques of elastic recoil detection analysis, Rutherford backscattering and resonance scattering, and scanning electron microscopy. Correlation of the result was made with Fourier Transform infrared spectroscopy.

The results of the ion beam analysis has identified oxygen as probably the only light element impurity in both hydrogenated amorphous silicon and nanocrystalline silicon powder at a concentration varying between 2 - 6 at %. In hydrogenated amorphous silicon, deposited at higher temperature (500°C), it was revealed that the impurity is only present in near the surface region of the material, while the contaminant is uniformly distributed throughout material deposited at a lower temperature of 350°C. The contamination of this impurity in the material might be attributable to exposure to air and also during growth in the case of a-Si:H. Samples Mw136 and Mw145, show the vulnerability of the deposited material to impurities.

The total hydrogen content is observed to average around 10% irrespective of the growth temperature, which strongly suggests that, this is determined by the flux of hydrogen during the deposition process. This is in turn determined only by the gas parameters.

Furthermore, the hydrogen content in as-deposited a-Si:H was seen to decrease when illuminated for four hours, continuing for eight hours illumination. The correlation made with FTIR revealed the shifting and formation of additional vibrational modes that signified formation of hydride and di-hydride complexes, which implies that there is formation of more dangling bonds in the material.

The hydrogen content analysed by ERDA showed higher atomic percentages than that given by FTIR because the ERDA measured the total hydrogen content while FTIR measured the bonded hydrogen.

The hydrogen content in the silicon nanoparticles is lower than for the a-Si:H layer. Furthermore, there is no significant change on the exposure to air for one week. This suggests that the particles are highly crystalline and compact, and that the hydrogen is in the bulk particles.

ACKNOWLEDGMENTS

I am grateful to Almighty God for this opportunity made available to me and I would like to express my profound gratitude to the following people for their contributions in various capacities to the successful completion of this work:

- Prof. C. M Comrie, Prof. D. T Britton and Prof. M. Härting for their unrelenting support and encouragement during this research work.

- Dr. Chris Theron for his guidance and making himself available whenever the need arises.

- My colleagues in the Solid State Research Group, they are wonderful people, for the moral and academic support.

- Mr. A. E. Odo and A. T. Raji for going through this period and sharing every moment of joy or otherwise together. I must say, indeed it is a wonderful experience.

- All the staff members of the Physics Department and Material Research Group, iThemba LABS for their good working relations

Most importantly, my wife and children for their co-operation and endurance while staying away from them for this period of studies.

Thank you all!

REFRERENCES

[1] Pere Rocai Cabarrocos, Anna Fontcuberta I Morral, Sarra Lebid and Yves Poissant. Pure Appl. Chem. **74** **(3)** (2001) 359

[2] R. E. I Schropp, B. Stannwoski, A. M Brockhoff, P.A.T.T Van Veenendaal and J. T. Rath. Mater. Phys. Mech. **1**. (2000) 73

[3] R. Biswas and Y-P Li. Physical Review Lett. **82** (1999) 12

[4] A. Kolodziej. J. Optoelectronics **12** **(1)** (2004) 21

[5] Amorphous silicon, edited by Kazuholu Tanaka, Elichi Maruyama, Toshikazu Shimada, Hiroaki Okamota. Translated by Takeshi Sato (National Institute for Advance Interdisciplinary Research, Ibaraki Japan.) 1999.

[6] Kuzua Morgaki, *Physics of Amorphous Semiconductors*. Imperial college Press. (1999) 51

[7] The Physics of Hydrogenated Amorphous silicon I, edited by J.D Joannopous and G. Lucovsky. (Structure, Preparation and Devices) Springer -Verlag. **55** (1984)

[8] H. M. Branz. Physical Review B **59** (1999) 5498

[9] M. Stutzmann, W. B. Jackson and C. C Tsai. Physical Review B **32,** (1985) 23

[10] G. Ledoux, O. Guillois, F Huisken B, Kohn D, Portenat C Reynard. Astronomy and Astrophysics **377** (2001) 707

[11] C. R. M Grovenor. Material for Semiconductor Devices. The Bath Press. England. 1987.

[12] C. Kittel. Introduction to Solid state Physics, John Willey & Sons (1971)

[13] The Physics of Hydrogenated Amorphous silicon II, edited by J.D Joannopous and G. Lucovsky. (Structure, Preparation and Devices) Springer-Verlag. **56** (1984)

[14] http://www.asi-net .net/asi.htm

[15] Hans J. Fecht, Formation of nanostructures by mechanical attrition: In Nanomaterials: Synthesis, Propeties and Application. A.S Edelstein and R.C cammarata (eds.). Institute of Physics Publishing. Bristol (2002).

[16] S. Thompson, C. R Perrey, C. B Carter, T. J. Belich, J. Kakalios and Uwe Kortshagen. J. Appl. Phys **97** (2005) 034310

[17] K. Brühne, M. B. Schubert, C. Köhler, and J. H Werner. Thin Solid film **395** (2001) 163

[18] Gan-Moog Chow and Lynn K. Kurihara. Chemical Sythensis and processing of nanostructure powders and films. In Nanostructured materials – Processing, Properties and Potentials Application. Koch, C.C (ed). Williams Andrew Publishing press (2002).

[19] K. E Gonsalves, S. P Rangarajan, J. Wang. Synthesis and Processing. In Handbook of nanostructure Vol. 1 Hari Singh Nalwa (ed). Academic Press, San Diego USA.

[20] Richard K. Baldwin, Katherine A. Pettigrew, Eva Ratai, Mattew P. Augustine and Susan M Kauzlarich . Chem. Commu. (2002) 1822

[21] H. Matsumura, J. Appl. Phys. **65** (1989) 4396

[22] A. M Mahan, J. Carapella, B.P Nelson, R.S Crandall nd Balberg. J. Appl, Phys. **69** (1991) 6728

[23] Moon-Sook Leek and Stacey F. Bent; J. Appl. Phys. **87 (9)** (2000) 4600

[24] J. K. Rath, B. Stannowski, P.A.T.T Van Veenendaal, Marieke K Van Veen and R.E.I Schropp. Thin Solid Films **395** (2001) 320

[25] Jason Knowles Holt in *HWCVD of silicon and silicon nitride for photovoitaics experiments, simulation and application.* Ph.D Thesis. Califonia institute of technilogy. (2002)

[26] Atul Pant, T.W. F Russell, Marylin C. Huff, Roger Aporicio, Robert W. Birkmire. Industrial & Engineering Chemistry Research **40 (5)** (2001) 1377

[27] R. Zedlitz, F. Kessler and M. Heintze. J. Non-Cryst. Solids. **83** (1993) 164

[28] K. F Feenstra, R. E. I Schropp and W.F Van der Weg. J. App.Phys. **85 (9)** (1999) 6843

[29] R. Aporicio, R. W Birkmire, A. Pant, M. Huff, T. W. F Russell and M. Mauk;
Process, analysis and modelling of thin film silicon deposited by HWCVD.
Proc. 199th Electrochemical Society Mtg. (2001). 260

[30] E. Hellstern, Fetcht H. J, Fu Z. And W. L. Johnson. J. Appl. Phys. **65** (1989) 305

[31] S. Linderoth, Proceeding of the 22nd RISϕ International Symposium on Material Science. Science of Metastable and Nanocrystalline Alloys Structure, Properties and Modelling. RISϕ National Laboratory, Roskilde Denmark (2001) 69

[32] E. C. Michelson and J. David Cohen. Phys Rev. B. **41 (3)** (1990) 1529

[33] Z. Medunic, D. Gracia, I. Bogdanovic Radovic, and M Jaksic. Nucl. Instr. and Meth. B **190** (2000) 611

[34] G. Boudreault, R. G. Elliman, R. Grotzschel, S. C. Gujrathi, C. Jeynes, W. N. Lennard, E. Rauhala, T. Sajavaara, H. Timmers, Y.O. Wang, T. D.M Weijers: Proceedings of the 15th ion beam conference, July 15 – 20 2001 Cuirus, Australia.

[35] A. Climent-Font , L. Galan, E. Swietlick, A. Revuelta. J. Aerosol. Sci. Vol. **27**, Suppl. 1 (1996) S15

[36] P. Wei, T. Tixier, M. Chicoine , S. Francoeur, A. Mascarebas, T. Tiedje and F. Schiettekatte. Nucl. Instr. and Meth B. **219 – 220** (2004) 671

[37] L. Wang, H. S Reehal, F.L Martinez, E. San Andrés and Adel Prado. Semicond. Sci. Technol. **18** (2003) 633

[38] N. Tomozeiu, J.J Van Hapert, W.M Arnoldbik, E. E Van Faassen, A.M Vredenberg, F.N.P.M Habraken. J.Optelectronics and Advance Material **3 (2)** (2001) 563

[39] T.D.M Weijers, R.G Elliman, and H. Timmers. Nucl. Instr. and Meth. B **219-220** (2004) 680

[40] D. Gracin, P. Dubcek, H. Zorc and K. Juraic. Thin Solid Films. **459** (2004) 216

[41] C. Jeynes, N. P Barradas, P. K Marriott, G. Boudreault, M. Jenkin, E. Wander and R. P Webb: J. Phys. D: Appl. Phys. **36** (2003) 97

[42] M. Nastasi, J .W Mayer, J. K Hirvonen. Ion-Solid Interactions: Fundamentals and Applications. (Ed) D. R Clark, S. Suresh & I.M Ward IRS (1996) Cambridge University press.

[43] A. Climent-Font. Material Science Institute Nicolas Cabrera, Universidale Autonom Madrid. Http://www.uam.es/otroscentros/inc

[44] Http://www.iem.csic.es/nucexp

[45] L. C. Feldman, James W. Mayer. Fundamental Of Surface And Thin Film Analysis. Elsevier science publishing Co.NY. 1986.

[46] Scott M. Baumann. Rutherford Backscattering spectrometry, Charles Evans and associate, Sunnyvale Califonia.

[47] J. S Williams and J. M Poate . Ion Implantation and Beam Processing. Academic Press. New York. 1984.

[48] K. G. Malmquist. Radiation Physics and Chemistry **71** (2001) 817

[49] H. karl, I. Grosshans, A Wenzel, B Stritzeker, R. Claessen V.N Strocou, G.E Cirlin, V. A Egorov, N.K Polyakov, Yu.B samsonenko, D.V Denisov, V. M Ustinov and Z. H I Alferov: Nanotechnology. **13** (2002) 631

[50] W. K Chu, J. W. Mayer and M. A. Nicolet. Backscattering Spectroscopy. Academic Press, Florida, USA 1978.

[51] B. L. Doyle, and P. S Peercey. Appl. Phys. Lett. **34** (1979) 812

[52] J.C Barbour and B.L Doyle, Elastic Recoil Detection: In Handbook of Modern ion beam material analysis. Joseph R.Tesmer and Micheal Nastasi (eds.) Material research society, Pittsburgh, Pennsylvania. (1995).

[53] L.R Doolittle, Nucl. Instr. and Meth. B **9** (1985) 344

[54] D.K Avasthi and W. Assmann. Current Science, **80** (**12**) (2001). 1532

[55] R. Siegele, I. Orlic and D. D. Cohen. Proceedings of the 15th International conference on Ion beam Analysis 22-27 June 2001, Cairns, Australia.

[56] M. UDhayasankar, J. Kumar, P.Pamasamy, D.K. Avasthi, and D. Kabiraj. Cryst. Res. Technol. **35** (2000) 1173

[57] T. D. M Weijers, R. G. Elliman, and H.Timmers. Nucl. Instr. and Meth. B **219-220** (2004) 680

[58] Rutherford, E. Phil. Mag. **21** (1911) 699

[59] hppt://mse.lastate.edu./microscopy

[60] Operating Manual HWCVD system version 1.0

[61] hppt://www.tlabs.ac.za

[62] J. F Zeigler, J. P Biersack, SRIM2003. HTTP//WWW.SRIM.ORG

[63] hppt://emu0.emu.uct.ac.za

[64] T. E Levine, M. Nastasi, K. C Walter, J. R Tesmer, C. J. Maggiore. Nucl. Instr. and Meth. B **103** (1995) 359

[65] R. A Street, J. C Knights, and D.K. Biegelsen, Phys. Rev. B **19** (1978) 3027

[66] Bolko von Ronedern. Proceeeding of National Center for Photovoiltaics and Solar Program Review meeting 2003.

[67] M. Bianconi, F. Abel, J.C Banks, A. Climent-Font, C. Cohen, B.L Doyle, R.Lotti, G. Lulli, R. Nipoti, I. Vickridge, D. Walsh and E. Wendler. Nucl. Instr.and Meth. B **161-163** (2000) 293

[68] S. R. Jadkar, J. V. Sali, D. V. Musale, S. T Kshirsagar and M. G. Takwale. Solar Energy Material and Solar cells. **71** (2002) 153

[69] P. Danesh, B. Pantchev, K. Antonova, E. Liasrokapis, D. Cranbole, B. Schmidt and J. Baran. J. Phys. D: Appl. Phys. **37**. (2004) 249

[70] U. Kroll, J. Meier, A. Shah, S. Mikhailov and J. Weber. J. Appl Phys. **80** (**9**) (1996) 4971

[71] P. A. Fedders. Phys. Rev. B **61** (**23**) (2001) 797

[72] Z. Medunic, D. Gracia, I. Bogdanovic Radovic, and M Jaksic. Nucl. Instr. and Meth. B **190** (2000) 611

[73] T.D.M Weijers, K.Gaff, H. Timmers, T.R.Ophel, R.G. Elliman, Heavy ion ERD analysis of doped-silica films for integrated photonics. Accepted by Nucl. Instru. Meth.B.

[74] H. Timmers, T. D. M. Weijers, R. G. Elliman, J. Uribasterra, H. J Whitlow and E. –L. Sarwe. Nucl. Instr. and Meth. B **190** (2002) 428